



Universiteit Gent  
Faculteit Wetenschappen  
Vakgroep Fysica en Sterrenkunde

<sup>2</sup> No title yet

<sup>3</sup> No sub-title neither, obviously...

---

<sup>4</sup> Alexis Fagot

5



Thesis to obtain the degree of  
Doctor of Philosophy in Physics  
Academic years 2012-2017





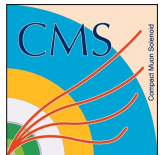


Universiteit Gent  
Faculteit Wetenschappen  
Vakgroep Fysica en Sterrenkunde

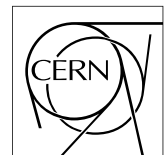
Promotoren: Dr. Michael Tytgat  
Prof. Dr. Dirk Ryckbosch

Universiteit Gent  
Faculteit Wetenschappen  
Vakgroep Fysica en Sterrenkunde  
Proeftuinstraat 86, B-9000 Gent, België  
Tel.: +32 9 264.65.28  
Fax.: +32 9 264.66.97

17



Thesis to obtain the degree of  
Doctor of Philosophy in Physics  
Academic years 2012-2017





## Acknowledgements

<sup>19</sup> Ici on remerciera tous les gens que j'ai pu croiser durant cette aventure et qui m'ont permis de passer  
<sup>20</sup> un bon moment

<sup>21</sup> *Gent, ici la super date de la mort qui tue de la fin d'écriture*  
<sup>22</sup> *Alexis Fagot*



# Table of Contents

23

|    |   |      |
|----|---|------|
| 24 | <b>Acknowledgements</b>   | i    |
| 25 | <b>Nederlandse samenvatting</b>   | xv   |
| 26 | <b>English summary</b>  | xvii |
| 27 | <b>1 Introduction</b>   | 1-1  |
| 28 | 1.1 A story of High Energy Physics . . . . .                                  | 1-1  |
| 29 | 1.2 Organisation of this study . . . . .                                      | 1-1  |
| 30 | <b>2 Investigating the TeV scale</b>  | 2-1  |
| 31 | 2.1 The Standard Model of Particle Physics . . . . .                          | 2-1  |
| 32 | 2.2 The Large Hadron Collider and the Compact Muon Solenoid . . . . .         | 2-1  |
| 33 | 2.3 Muon Phase-II Upgrade . . . . .   | 2-1  |
| 34 | <b>3 Amplification processes in gaseous detectors</b>                         | 3-1  |
| 35 | 3.1 Signal formation . . . . .  | 3-1  |
| 36 | 3.2 Gas transport parameters . . . . .  | 3-1  |
| 37 | <b>4 Resistive Plate Chambers</b>   | 4-1  |
| 38 | 4.1 Principle . . . . .   | 4-1  |
| 39 | 4.2 Rate capability of Resistive Plate Chambers . . . . .                     | 4-1  |
| 40 | 4.3 High time resolution . . . . .  | 4-1  |
| 41 | 4.4 Resistive Plate Chambers at CMS . . . . .                                 | 4-1  |
| 42 | 4.4.1 Overview . . . . .  | 4-1  |
| 43 | 4.4.2 The present RPC system . . . . .  | 4-2  |
| 44 | 4.4.3 Pulse processing of CMS RPCs . . . . .                                  | 4-3  |
| 45 | <b>5 Longevity studies and Consolidation of the present CMS RPC subsystem</b> | 5-1  |
| 46 | 5.1 Testing detectors under extreme conditions . . . . .                      | 5-1  |
| 47 | 5.1.1 The Gamma Irradiation Facilities . . . . .                              | 5-3  |
| 48 | 5.1.1.1 GIF . . . . .   | 5-3  |
| 49 | 5.1.1.2 GIF++ . . . . .   | 5-5  |
| 50 | 5.2 Preliminary tests at GIF . . . . .  | 5-7  |
| 51 | 5.2.1 Resistive Plate Chamber test setup . . . . .                            | 5-7  |
| 52 | 5.2.2 Data Acquisition . . . . .  | 5-9  |
| 53 | 5.2.3 Geometrical acceptance of the setup layout to cosmic muons . . . . .    | 5-9  |
| 54 | 5.2.3.1 Description of the simulation layout . . . . .                        | 5-10 |
| 55 | 5.2.3.2 Simulation procedure . . . . .  | 5-12 |
| 56 | 5.2.3.3 Results . . . . .   | 5-13 |
| 57 | 5.2.4 Photon flux at GIF . . . . .  | 5-13 |

---

|    |          |   |            |
|----|----------|---|------------|
| 58 | 5.2.4.1  | Expectations from simulations . . . . .                                 | 5-13       |
| 59 | 5.2.4.2  | Dose measurements . . . . .   | 5-18       |
| 60 | 5.2.5    | Results and discussions . . . . .                                       | 5-19       |
| 61 | 5.3      | Longevity tests at GIF++ . . . . .                                      | 5-20       |
| 62 | 5.3.1    | Description of the Data Acquisition . . . . .                           | 5-23       |
| 63 | 5.3.2    | RPC current, environmental and operation parameter monitoring . . . . . | 5-24       |
| 64 | 5.3.3    | Measurement procedure . . . . .   | 5-25       |
| 65 | 5.3.4    | Longevity studies results . . . . .                                     | 5-25       |
| 66 | <b>6</b> | <b>Investigation on high rate RPCs</b>                                  | <b>6-1</b> |
| 67 | 6.1      | Rate limitations and ageing of RPCs . . . . .                           | 6-1        |
| 68 | 6.1.1    | Low resistivity electrodes . . . . .                                    | 6-1        |
| 69 | 6.1.2    | Low noise front-end electronics . . . . .                               | 6-1        |
| 70 | 6.2      | Construction of prototypes . . . . .                                    | 6-1        |
| 71 | 6.3      | Results and discussions . . . . .                                       | 6-1        |
| 72 | <b>7</b> | <b>Conclusions and outlooks</b>   | <b>7-1</b> |
| 73 | 7.1      | Conclusions . . . . .   | 7-1        |
| 74 | 7.2      | Outlooks . . . . .  | 7-1        |
| 75 | <b>A</b> | <b>A data acquisition software for CAEN VME TDCs</b>                    | <b>A-1</b> |
| 76 | A.1      | GIF++ DAQ file tree . . . . .   | A-1        |
| 77 | A.2      | Usage of the DAQ . . . . .  | A-2        |
| 78 | A.3      | Description of the readout setup . . . . .                              | A-3        |
| 79 | A.4      | Data read-out . . . . .   | A-3        |
| 80 | A.4.1    | V1190A TDCs . . . . .   | A-4        |
| 81 | A.4.2    | DataReader . . . . .  | A-6        |
| 82 | A.5      | Communications . . . . .  | A-10       |
| 83 | A.5.1    | V1718 USB Bridge . . . . .  | A-10       |
| 84 | A.5.2    | Configuration file . . . . .  | A-11       |
| 85 | A.5.3    | WebDCS/DAQ intercommunication . . . . .                                 | A-15       |
| 86 | A.5.4    | Example of inter-process communication cycle . . . . .                  | A-16       |
| 87 | A.6      | Software export . . . . .   | A-16       |
| 88 | <b>B</b> | <b>Details on the offline analysis package</b>                          | <b>B-1</b> |
| 89 | B.1      | GIF++ Offline Analysis file tree . . . . .                              | B-1        |
| 90 | B.2      | Usage of the Offline Analysis . . . . .                                 | B-2        |
| 91 | B.2.1    | Output of the offline tool . . . . .                                    | B-3        |
| 92 | B.2.1.1  | ROOT file . . . . .   | B-3        |
| 93 | B.2.1.2  | CSV files . . . . .   | B-5        |
| 94 | B.3      | Analysis inputs and information handling . . . . .                      | B-6        |
| 95 | B.3.1    | Dimensions file and IniFile parser . . . . .                            | B-6        |
| 96 | B.3.2    | TDC to RPC link file and Mapping . . . . .                              | B-7        |
| 97 | <b>C</b> | <b>Structure of the hybrid simulation software</b>                      | <b>C-1</b> |
| 98 | C.1      | Introduction . . . . .  | C-1        |

# List of Figures

99

|              |   |     |
|--------------|---|-----|
| 100      2.1 | Absorbed dose in the CMS cavern after an integrated luminosity of 3000 fb. R is the transverse distance from the beamline and Z is the distance along the beamline from the Interaction Point at Z=0. . . . .   | 2-2 |
| 101      2.2 | A quadrant of the muon system, showing DTs (yellow), RPCs (light blue), and CSCs (green). The locations of new forward muon detectors for Phase-II are contained within the dashed box and indicated in red for GEM stations (ME0, GE1/1, and GE2/1) and dark blue for improved RPC (iRPC) stations (RE3/1 and RE4/1). . . . .  | 2-2 |
| 102      2.3 | RMS of the multiple scattering displacement as a function of muon $p_T$ for the proposed forward muon stations. All of the electromagnetic processes such as bremsstrahlung and magnetic field effect are included in the simulation. . . . .   | 2-3 |
| 103      4.1 | Signals from the RPC strips are shaped by the FEE described on Figure 4.1a. Output LVDS signals are then read-out by a TDC module connected to a computer or converted into NIM and sent to scalers. Figure 4.1b describes how these converted signals are put in coincidence with the trigger. . . . .   | 4-3 |
| 104      4.2 | Description of the principle of a CFD. A comparison of threshold triggering (left) and constant fraction triggering (right) is shown in Figure 4.2a. Constant fraction triggering is obtained thanks to zero-crossing technique as explained in Figure 4.2b. The signal arriving at the input of the CFD is split into three components. A first one is delayed and connected to the inverting input of a first comparator. A second component is connected to the noninverting input of this first comparator. A third component is connected to the noninverting input of another comparator along with a threshold value connected to the inverting input. Finally, the output of both comparators is fed through an AND gate. . . . . | 4-4 |
| 105      5.1 | (5.1a) Extrapolation from 2016 data of single hit rate per unit area in the barrel region. (5.1b) Extrapolation from 2016 data of single hit rate per unit area in the endcap region. . . . .   | 5-2 |
| 106      5.2 | Background Fluka simulation compared to 2016 Data at $L = 10^{34} \text{ cm}^{-2} \cdot \text{s}^{-1}$ in the fourth endcap disk region. A mismatch in between simulation and data can be observed. [To be understood.] . . . . .   | 5-3 |
| 107      5.3 | Layout of the test beam zone called X5c GIF at CERN. Photons from the radioactive source produce a sustained high rate of random hits over the whole area. The zone is surrounded by 8 m high and 80 cm thick concrete walls. Access is possible through three entry points. Two access doors for personnel and one large gate for material. A crane allows installation of heavy equipment in the area. . . . .  | 5-4 |
| 108      5.4 | $^{137}\text{Cs}$ decays by $\beta^-$ emission to the ground state of $^{137}\text{Ba}$ (BR = 5.64%) and via the 662 keV isomeric level of $^{137}\text{Ba}$ (BR = 94.36%) whose half-life is 2.55 min. . . . .   | 5-5 |

---

|     |      |   |      |
|-----|------|---|------|
| 136 | 5.5  | Floor plan of the GIF++ facility. When the facility downstream of the GIF++ takes electron beam, a beam pipe is installed along the beam line (z-axis). The irradiator can be displaced laterally (its center moves from $x = 0.65$ m to 2.15 m), to increase the distance to the beam pipe. . . . .  | 5-5  |
| 140 | 5.6  | Simulated unattenuated current of photons in the xz plane (Figure 5.6a) and yz plane (Figure 5.6b) through the source at $x = 0.65$ m and $y = 0$ m. With angular correction filters, the current of 662 keV photons is made uniform in xy planes. . . . .  | 5-6  |
| 143 | 5.7  | Description of the RPC setup. Dimensions are given in mm. A tent containing RPCs is placed at 1720 mm from the source container. The source is situated in the center of the container. RE-4-2-BARC-161 chamber is 160 mm inside the tent. This way, the distance between the source and the chambers plan is 2060 mm. Figure 5.7a provides a side view of the setup in the xz plane while Figure 5.7b shows a top view in the yz plane. . . . .  | 5-7  |
| 149 | 5.8  | RE-4-2-BARC-161 chamber is inside the tent as described in Figure 5.7. In the top right, the two scintillators used as trigger can be seen. This trigger system has an inclination of 10° relative to horizontal and is placed above half-partition B2 of the RPCs. PMT electronics are shielded thanks to lead blocks placed in order to protect them without stopping photons from going through the scintillators and the chamber. . . . .   | 5-8  |
| 154 | 5.9  | Hit distributions over all 3 partitions of RE-4-2-BARC-161 chamber is showed on these plots. Top, middle and bottom figures respectively correspond to partitions A, B, and C. These plots show that some events still occur in other half-partitions than B2, which corresponds to strips 49 to 64, in front of which the trigger is placed, contributing to the inefficiency of detection of cosmic muons. In the case of partitions A and C, the very low amount of data can be interpreted as noise. On the other hand, it is clear that a little portion of muons reach the half-partition B1, corresponding to strips 33 to 48. . . . . | 5-9  |
| 162 | 5.10 | Results are derived from data taken on half-partition B2 only. On the 18 <sup>th</sup> of June 2014, data has been taken on chamber RE-2-BARC-161 at building 904 (Prevessin Site) with cosmic muons providing us a reference efficiency plateau of $(97.54 \pm 0.15)\%$ represented by a black curve. A similar measurement has been done at GIF on the 21 <sup>st</sup> of July with the same chamber giving a plateau of $(78.52 \pm 0.94)\%$ represented by a red curve. . . . .  | 5-10 |
| 168 | 5.11 | Representation of the layout used for the simulations of the test setup. The RPC is represented as a yellow trapezoid while the two scintillators as blue cuboids looking at the sky. A green plane corresponds to the muon generation plane within the simulation. Figure 5.7a shows a global view of the simulated setup. Figure 5.7b shows a zommed view that allows to see the 2 scintillators as well as the full RPC plane. . . . .   | 5-11 |
| 173 | 5.12 | $\gamma$ flux $F(D)$ is plot using values from table 5.1. As expected, the plot shows similar attenuation behaviours with increasing distance for each absorption factors. . . . .  | 5-14 |
| 175 | 5.13 | Figure 5.13a shows the linear approximation fit done via formulae 5.7 on data from table 5.2. Figure 5.13b shows a comparison of this model with the simulated flux using a and b given in figure 5.13a in formulae 5.4 and the reference value $D_0 = 50\text{cm}$ and the associated flux for each absorption factor $F_0^{ABS}$ from table 5.1 . . . . .   | 5-16 |
| 179 | 5.14 | Dose measurements has been done in a plane corresponding to the tents front side. This plan is 1900 mm away from the source. As explained in the first chapter, a lens-shaped lead filter provides a uniform photon flux in the vertical plan orthogonal to the beam direction. If the second line of measured fluxes is not taken into account because of lower values due to experimental equipments in the way between the source and the tent, the uniformity of the flux is well showed by the results. . . . .  | 5-18 |

---

|     |  |      |
|-----|--|------|
| 185 | 5.15 . . . . .   | 5-19 |
| 186 | 5.16 Evolution of the maximum efficiency for RE2 (5.16a) and RE4 (5.16b) chambers  |      |
| 187 | with increasing extrapolated $\gamma$ rate per unit area at working point. Both irradiated   |      |
| 188 | (blue) and non irradiated (red) chambers are shown. . . . .  | 5-21 |
| 189 | 5.17 Evolution of the working point for RE2 (5.17a) and RE4 (5.17b) with increasing  |      |
| 190 | extrapolated $\gamma$ rate per unit area at working point. Both irradiated (blue) and non  |      |
| 191 | irradiated (red) chambers are shown. . . . .   | 5-21 |
| 192 | 5.18 Evolution of the maximum efficiency at HL-LHC conditions, i.e. a background hit   |      |
| 193 | rate per unit area of 300 Hz/cm <sup>2</sup> , with increasing integrated charge for RE2 (5.18a)                                   |      |
| 194 | and RE4 (5.18b) detectors. Both irradiated (blue) and non irradiated (red) chambers  |      |
| 195 | are shown. The integrated charge for non irradiated detectors is recorded during test  |      |
| 196 | beam periods and stays small with respect to the charge accumulated in irradiated  |      |
| 197 | chambers. . . . .  | 5-22 |
| 198 | 5.19 Comparison of the efficiency sigmoid before (triangles) and after (circles) irradiation                                       |      |
| 199 | for RE2 (5.19a) and RE4 (5.19b) detectors. Both irradiated (blue) and non irradiated   |      |
| 200 | (red) chambers are shown. . . . .  | 5-22 |
| 201 | 5.20 Evolution of the Bakelite resistivity for RE2 (5.20a) and RE4 (5.20b) detectors. Both   |      |
| 202 | irradiated (blue) and non irradiated (red) chambers are shown. . . . .   | 5-23 |
| 203 | 5.21 Evolution of the noise rate per unit area for the irradiated chamber RE2-2-BARC-9   |      |
| 204 | only. . . . .  | 5-23 |
| 205 | A.1 (A.1a) View of the front panel of a V1190A TDC module [10]. (A.1b) View of the   |      |
| 206 | front panel of a V1718 Bridge module [11]. (A.1c) View of the front panel of a 6U  |      |
| 207 | 6021 VME crate [12]. . . . .   | A-3  |
| 208 | A.2 Module V1190A <i>Trigger Matching Mode</i> timing diagram [10]. . . . .  | A-4  |
| 209 | A.3 Structure of the ROOT output file generated by the DAQ. The 5 branches ( <code>EventNumber</code> ,                            |      |
| 210 | <code>number_of_hits</code> , <code>Quality_flag</code> , <code>TDC_channel</code> and <code>TDC_TimeStamp</code> ) are visible on |      |
| 211 | the left panel of the ROOT browser. On the right panel is visible the histogram cor-   |      |
| 212 | responding to the variable <code>nHits</code> . In this specific example, there were approximately                                 |      |
| 213 | 50k events recorded to measure the gamma irradiation rate on the detectors. Each   |      |
| 214 | event is stored as a single entry in the <code>TTree</code> . . . . .  | A-10 |
| 215 | A.4 WebDCS DAQ scan page. On this page, shifters need to choose the type of scan   |      |
| 216 | (Rate, Efficiency or Noise Reference scan), the gamma source configuration at the  |      |
| 217 | moment of data taking, the beam configuration, and the trigger mode. These in-   |      |
| 218 | formation will be stored in the DAQ ROOT output. Are also given the minimal  |      |
| 219 | measurement time and waiting time after ramping up of the detectors is over before   |      |
| 220 | starting the data acquisition. Then, the list of HV points to scan and the number of   |      |
| 221 | triggers for each run of the scan are given in the table underneath. . . . .   | A-12 |



## List of Tables

222

|              |   |      |
|--------------|---|------|
| 223      5.1 | Total photon flux ( $E\gamma \leq 662$ keV) with statistical error predicted considering a<br>224 $^{137}\text{Cs}$ activity of 740 GBq at different values of the distance $D$ to the source along<br>225      the x-axis of irradiation field [6]. . . . .  | 5-13 |
| 226      5.2 | Correction factor $c$ is computed thanks to formulae 5.5 taking as reference $D_0 =$<br>227      50 cm and the associated flux $F_0^{ABS}$ for each absorption factor available in table 5.1. . . . .   | 5-15 |
| 228      5.3 | The data at $D_0$ in 1997 is taken from [6]. In a second step, using Equations 5.8<br>229      and 5.9, the flux at $D$ can be estimated in 1997. Then, taking into account the<br>230      attenuation of the source activity, the flux at $D$ can be estimated at the time of the<br>231      tests in GIF in 2014. Finally, assuming a sensitivity of the RPC to $\gamma$ $s = 2 \cdot 10^{-3}$ ,<br>232      an estimation of the hit rate per unit area is obtained. . . . . | 5-17 |
| 233      A.1 | Inter-process communication cycles in between the webDCS and the DAQ through<br>234      file string signals. . . . .   | A-17 |



235

## List of Acronyms

236

### List of Acronyms

237

238

#### A

239

240

241

AFL

Almost Full Level

242

243

#### B

244

245

246 BARC

Bhabha Atomic Research Centre

247 BLT

Block Transfer

248 BR

Branching Ratio

249

250

#### C

251

252

253 CAEN

Costruzioni Apparecchiature Elettroniche Nucleari S.p.A.

254 CERN

European Organization for Nuclear Research

255 CFD

Constant Fraction Discriminator

256 CMS

Compact Muon Solenoid

257 CSC

Cathode Strip Chamber

258

259

#### D

260

261

262 DAQ

Data Acquisition

263 DCS

Detector Control Software

264 DQM

Data Quality Monitoring

265 DT

Drift Tube

266

267

#### F

268

269

|     |          |  |
|-----|----------|--|
| 270 | FEE      | Front-End Electronics  |
| 271 | FEB      | Front-End Board  |
| 272 |          |  |
| 273 | <b>G</b> |  |
| 274 |          |  |
| 275 |          |  |
| 276 | GE-/-    | Find a good description  |
| 277 | GE1/1    | Find a good description  |
| 278 | GE2/1    | Find a good description  |
| 279 | GEANT    | GEometry ANd Tracking - a series of software toolkit platforms developed by CERN |
| 280 |          |  |
| 281 | GEM      | Gas Electron Multiplier  |
| 282 | GIF      | Gamma Irradiation Facility   |
| 283 | GIF++    | new Gamma Irradiation Facility   |
| 284 |          |  |
| 285 | <b>H</b> |  |
| 286 |          |  |
| 287 |          |  |
| 288 | HL-LHC   | High Luminosity LHC  |
| 289 | HV       | High Voltage   |
| 290 |          |  |
| 291 | <b>I</b> |  |
| 292 |          |  |
| 293 |          |  |
| 294 | iRPC     | improved RPC   |
| 295 | IRQ      | Interrupt Request  |
| 296 |          |  |
| 297 | <b>L</b> |  |
| 298 |          |  |
| 299 |          |  |
| 300 | LHC      | Large Hadron Collider  |
| 301 | LS1      | First Long Shutdown  |
| 302 | LS3      | Third Long Shutdown  |
| 303 | LV       | Low Voltage  |
| 304 | LVDS     | Low-Voltage Differential Signaling   |
| 305 |          |  |
| 306 | <b>M</b> |  |
| 307 |          |  |
| 308 |          |  |
| 309 | MC       | Monte Carlo  |
| 310 | MCNP     | Monte Carlo N-Particle   |
| 311 | ME-/-    | Find good description  |
| 312 | ME0      | Find good description  |

|     |          |  |
|-----|----------|--|
| 313 |          |  |
| 314 |          |  |
| 315 | <b>N</b> |  |
| 316 |          |  |
| 317 | NIM      | Nuclear Instrumentation Module logic signals |
| 318 |          |  |
| 319 | <b>P</b> |  |
| 320 |          |  |
| 321 |          |  |
| 322 | PMT      | PhotoMultiplier Tube                         |
| 323 |          |  |
| 324 |          |  |
| 325 | <b>R</b> |  |
| 326 |          |  |
| 327 | RE-/-    | Find a good description                      |
| 328 | RE2/2    | Find a good description                      |
| 329 | RE3/1    | Find a good description                      |
| 330 | RE3/2    | Find a good description                      |
| 331 | RE4/1    | Find a good description                      |
| 332 | RE4/2    | Find a good description                      |
| 333 | RE4/3    | Find a good description                      |
| 334 | RMS      | Root Mean Square                             |
| 335 | ROOT     | a framework for data processing born at CERN |
| 336 | RPC      | Resistive Plate Chamber                      |
| 337 |          |  |
| 338 |          |  |
| 339 | <b>S</b> |  |
| 340 |          |  |
| 341 | SPS      | Super Proton Synchrotron                     |
| 342 |          |  |
| 343 |          |  |
| 344 | <b>T</b> |  |
| 345 |          |  |
| 346 | TDC      | Time-to-Digital Converter                    |
| 347 |          |  |
| 348 |          |  |
| 349 | <b>W</b> |  |
| 350 |          |  |
| 351 | webDCS   | Web Detector Control System                  |



353

## Nederlandse samenvatting –Summary in Dutch–

355 Le resume en Neerlandais (j'aurais peut-être de apprendre la langue juste pour ca...).

354



## English summary

<sup>357</sup> Le meme résume mais en Anglais (on commencera par la hein!).



# 1

## Introduction

358

359

<sup>360</sup> **1.1 A story of High Energy Physics**

<sup>361</sup> **1.2 Organisation of this study**



# 2

362

363

## Investigating the TeV scale

364 **2.1 The Standard Model of Particle Physics**

365 **2.2 The Large Hadron Collider and the Compact Muon Solenoid**

366 **2.3 Muon Phase-II Upgrade**

367 After the more than two years lasting First Long Shutdown (LS1), the Large Hadron Collider (LHC)  
368 delivered its very first Run-II proton-proton collisions early 2015. LS1 gave the opportunity to the  
369 LHC and to the its experiments to undergo upgrades. The accelerator is now providing collisions  
370 at center-of-mass energy of 13 TeV and bunch crossing rate of 40 MHz, with a peak luminosity  
371 exceeding its design value. During the first and upcoming second LHC Long Shutdown, the Compact  
372 Muon Solenoid (CMS) detector is also undergoing a number of upgrades to maintain a high system  
373 performance [1].

374 From the LHC Phase-2 or High Luminosity LHC (HL-LHC) period onwards, i.e. past the Third  
375 Long Shutdown (LS3), the performance degradation due to integrated radiation as well as the average  
376 number of inelastic collisions per bunch crossing, or pileup, will rise substantially and become a  
377 major challenge for the LHC experiments, like CMS that are forced to address an upgrade program  
378 for Phase-II [2]. Simulations of the expected distribution of absorbed dose in the CMS detector  
379 under HL-LHC conditions, show in figure 5.14 that detectors placed close to the beamline will have  
380 to withstand high irradiation, the radiation dose being of the order of a few tens of Gy.

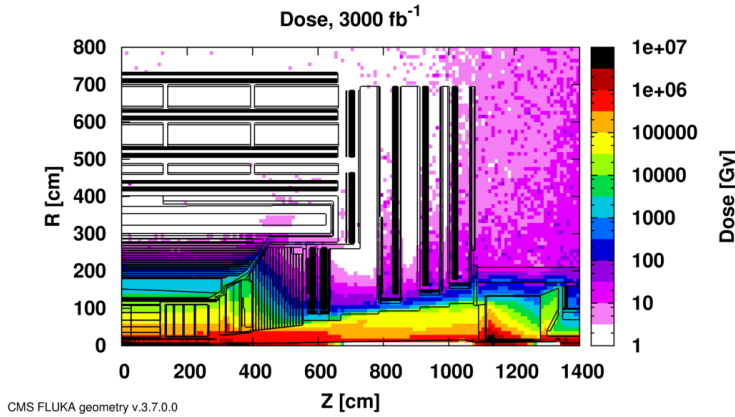


*Figure 2.1: Absorbed dose in the CMS cavern after an integrated luminosity of 3000 fb<sup>-1</sup>. R is the transverse distance from the beamline and Z is the distance along the beamline from the Interaction Point at Z=0.*

381     The measurement of small production cross-section and/or decay branching ratio processes, such  
 382     as the Higgs boson coupling to charge leptons or the  $B_s \rightarrow \mu^+\mu^-$  decay, is of major interest and  
 383     specific upgrades in the forward regions of the detector will be required to maximize the physics  
 384     acceptance on the largest possible solid angle. To ensure proper trigger performance within the  
 385     present coverage, the muon system will be completed with new chambers. In figure 2.2 one can  
 386     see that the existing Cathode Strip Chambers (CSCs) will be completed by Gas Electron Multipliers  
 387     (GEMs) and Resistive Plate Chambers (RPCs) in the pseudo-rapidity region  $1.6 < |\eta| < 2.4$  to  
 388     complete its redundancy as originally scheduled in the CMS Technical Proposal [3].

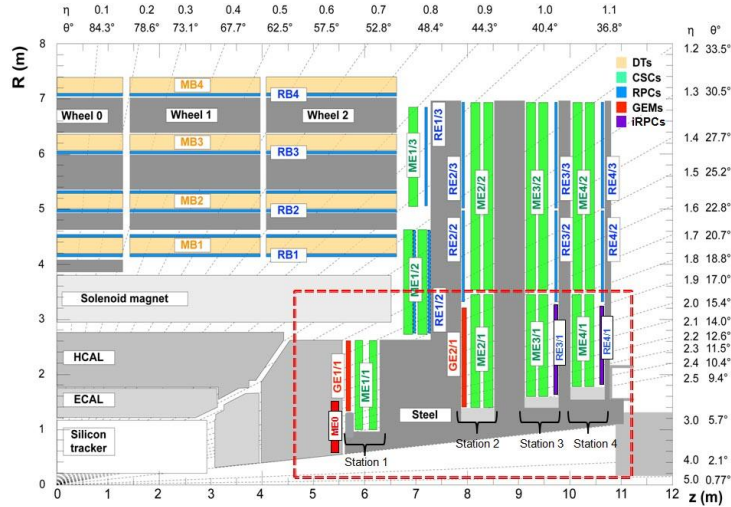


*Figure 2.2: A quadrant of the muon system, showing DTs (yellow), RPCs (light blue), and CSCs (green). The locations of new forward muon detectors for Phase-II are contained within the dashed box and indicated in red for GEM stations (MEO, GE1/1, and GE2/1) and dark blue for improved RPC (iRPC) stations (RE3/1 and RE4/1).*

389     RPCs are used by the CMS first level trigger for their good timing performances. Indeed, a very

good bunch crossing identification can be obtained with the present CMS RPC system, given their fast response of the order of 1 ns. In order to contribute to the precision of muon momentum measurements, muon chambers should have a spatial resolution less or comparable to the contribution of multiple scattering [1]. Most of the plausible physics is covered only considering muons with  $p_T < 100$  GeV thus, in order to match CMS requirements, a spatial resolution of  $\mathcal{O}(\text{few mm})$  the proposed new RPC stations, as shown by the simulation in figure 2.3. According to preliminary designs, RE3/1 and RE4/1 readout pitch will be comprised between 3 and 6 mm and 5  $\eta$ -partitions could be considered.

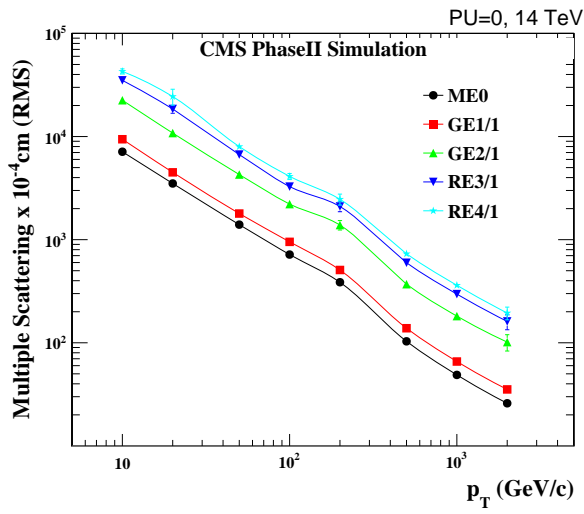


Figure 2.3: RMS of the multiple scattering displacement as a function of muon  $p_T$  for the proposed forward muon stations. All of the electromagnetic processes such as bremsstrahlung and magnetic field effect are included in the simulation.



# 3

398

399

## Amplification processes in gaseous detectors

400 **3.1 Signal formation**

401 **3.2 Gas transport parameters**



# 4

402

403

## Resistive Plate Chambers

404 **4.1 Principle**

405 **4.2 Rate capability of Resistive Plate Chambers**

406 **4.3 High time resolution**

407 **4.4 Resistive Plate Chambers at CMS**

408 **4.4.1 Overview**

409 The Resistive Plate Chambers (RPC) system, located in both barrel and endcap regions, provides a  
410 fast, independent muon trigger with a looser  $p_T$  threshold over a large portion of the pseudorapidity  
411 range ( $|\eta| < 1.6$ ) [add reconstruction].

412

413 During High-Luminosity LHC (HL-LHC) operations the expected conditions in terms of back-  
414 ground and pile-up will make the identification and correct  $P_T$  assignment a challenge for the Muon  
415 system. The goal of RPC upgrade is to provide additional hits to the Muon system with precise tim-  
416 ing. All these informations will be elaborated by the trigger system in a global way enhancing the  
417 performance of the trigger in terms of efficiency and rate control. The RPC Upgrade is based on two  
418 projects: an improved Link Board System and the extension of the RPC coverage up to  $|\eta| = 2.4$ .  
419 [FIXME 2.4 or 2.5?]

420 The Link Board system, that will be described in section xxx, is responsible to process, syn-  
421 chronize and zero-suppress the signals coming from the RPC front end boards. The Link Board  
422 components have been produced between 2006 and 2007 and will be subjected to aging and failure  
423 in the long term. The upgraded Link Board system will overcome the aging problems described in  
424 section xxx and will allow for a more precise timing information to the RPC hits from 25 to 1 ns [ref  
425 section xxx].

426 The extension of the RPC system up to  $|\eta| = 2.1$  was already planned in the CMS TDR [ref  
 427 cmstdr] and staged because of budget limitations and expected background rates higher than the rate  
 428 capability of the present CMS RPCs in that region. An extensive R&D program has been done in  
 429 order to develop an improved RPC that fulfills the CMS requirements. Two new RPC layers in the  
 430 innermost ring of stations 3 and 4 will be added with benefits to the neutron-induced background  
 431 reduction and efficiency improvement for both trigger and offline reconstruction.

#### 432 4.4.2 The present RPC system

433 The RPC system is organized in 4 stations called RB1 to RB4 in the barrel region, and RE1 to RE4  
 434 in the endcap region. The innermost barrel stations, RB1 and RB2, are instrumented with 2 layers  
 435 of RPCs facing the innermost (RB1in and RB2in) and outermost (RB1out and RB2out) sides of the  
 436 DT chambers. Every chamber is then divided from the read-out point of view into 2 or 3  $\eta$  partitions  
 437 called “rolls”. The RPC system consist of 480 barrel chambers and 576 endcap chambers. Details  
 438 on the geometry are discussed in the paper [ref to geo paper].

439 The CMS RPC chamber is a double-gap, operated in avalanche mode to ensure reliable operation  
 440 at high rates. Each RPC gap consists of two 2-mm-thick resistive High-Pressure Laminate (HPL)  
 441 plates separated by a 2-mm-thick gas gap. The outer surface of the HPL plates is coated with a thin  
 442 conductive graphite layer, and a voltage is applied. The RPCs are operated with a 3-component,  
 443 non-flammable gas mixture consisting of 95.2% freon ( $C_2H_2F_4$ , known as R134a), 4.5% isobutane  
 444 ( $i-C_4H_{10}$ ), and 0.3% sulphur hexafluoride ( $SF_6$ ) with a relative humidity of 40% - 50%. Readout  
 445 strips are aligned in  $\eta$  between the 2 gas gaps. [\[Add a sentence on FEBs.\]](#)

446 The discriminated signals coming from the Front End boards feed via twisted cables (10 to 20 m  
 447 long) the Link Board System located in UXC on the balconies around the detector. The Link System  
 448 consist of the 1376 Link Boards (LBs) and the 216 Control Boards (CBs), placed in 108 Link Boxes.  
 449 The Link Box is a custom crate (6U high) with 20 slots (for two CBs and eighteen LBs). The Link  
 450 Box contains custom backplane to which the cables from the chambers are connected, as well as the  
 451 cables providing the LBs and CBs power supply and the cables for the RPC FEBs control with use  
 452 of the I2C protocol (trough the CB). The backplane itself contains only connectors (and no any other  
 453 electronic devices).

454 The Link Board has 96 input channels (one channel corresponds to one RPC strip). The input  
 455 signals are the  $\sim 100$  ns binary pulses which are synchronous to the RPC hits, but not to the LHC  
 456 clock (which drives the entire CMS electronics). Thus the first step of the FEB signals processing  
 457 is synchronization, i.e. assignment of the signals to the BXes (25 ns periods). Then the data are  
 458 compressed with a simple zero-suppressing algorithm (the input channels are grouped into 8 bit  
 459 partitions, only the partitions with at least one nonzero bit are selected for each BX). Next, the non-  
 460 empty partitions are time-multiplexed i.e. if there are more than one such partition in a given BX,  
 461 they are sent one-by-one in consecutive BXes. The data from 3 neighbouring LBs are concentrated  
 462 by the middle LB which contains the optical transmitter for sending them to the USC over a fiber at  
 463 1.6 Gbps.

464 The Control Boards provide the communication of the control software with the LBs via the  
 465 FEC/CCU system. The CBs are connected into token rings, each ring consists of 12 CBs of one  
 466 detector tower and a FEC mezzanine board placed on the CCS board located in the VME crate in  
 467 the USC. In total, there are 18 rings in the entire Link System. The CBs also perform automatic  
 468 reloading of the LB's firmware which is needed in order to avoid accumulation of the radiation  
 469 induced SEUs in the LBs firmware.

470 Both LBs and CB are based on the Xilinx Spartan III FPGAs, the CB additionally contains  
 471 radiation-tolerant (FLASH based) FPGA Actel ProAsicPlus.

472 The High Voltage power system is located in USC, not exposed to radiation and easily accessible  
 473 for any reparation. A single HV channel powers 2 RPC chambers both in the barrel and endcap  
 474 regions. The Low Voltage boards are located in UXC on the balconies and provide the voltage to the  
 475 front end electronics.

#### 476 4.4.3 Pulse processing of CMS RPCs

477 Signals induced by cosmic particle in the RPC strips are shaped by standard CMS RPC Front-End  
 478 Electronics (FEE) following the scheme of Figure 4.1. On a first stage, analogic signals are amplified  
 479 and then sent to the Constant Fraction Discriminator (CFD) described in Figure 4.2. At the end of  
 480 the chain, 100 ns long pulses are sent in the LVDS output. These output signal are sent on one side to  
 481 a V1190A Time-to-Digital Converter (TDC) module from CAEN and on the other to an OR module  
 482 to count the number of detected signals. Trigger and hit coïncidences are monitored using scalers.  
 483 The TDC is used to store the data into ROOT files. These files are thus analysed to understand the  
 484 detectors performance.

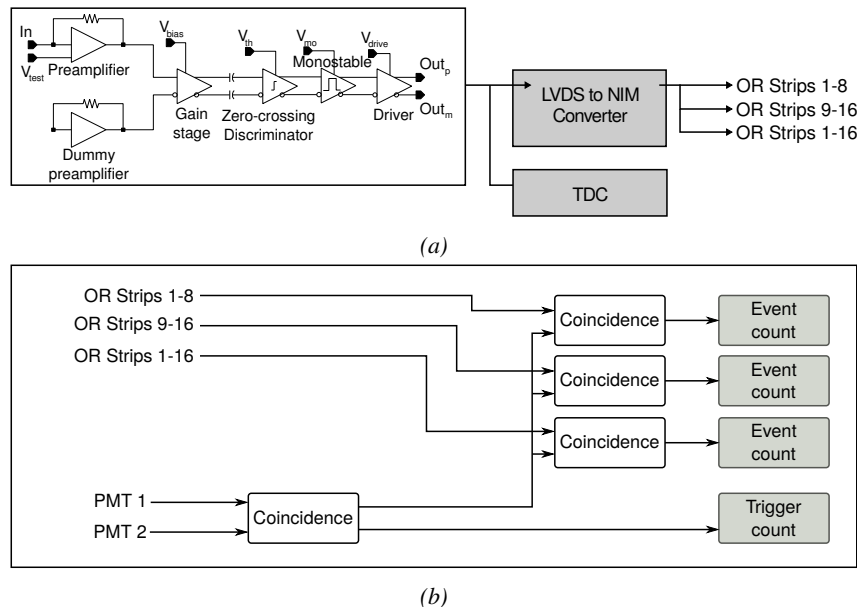
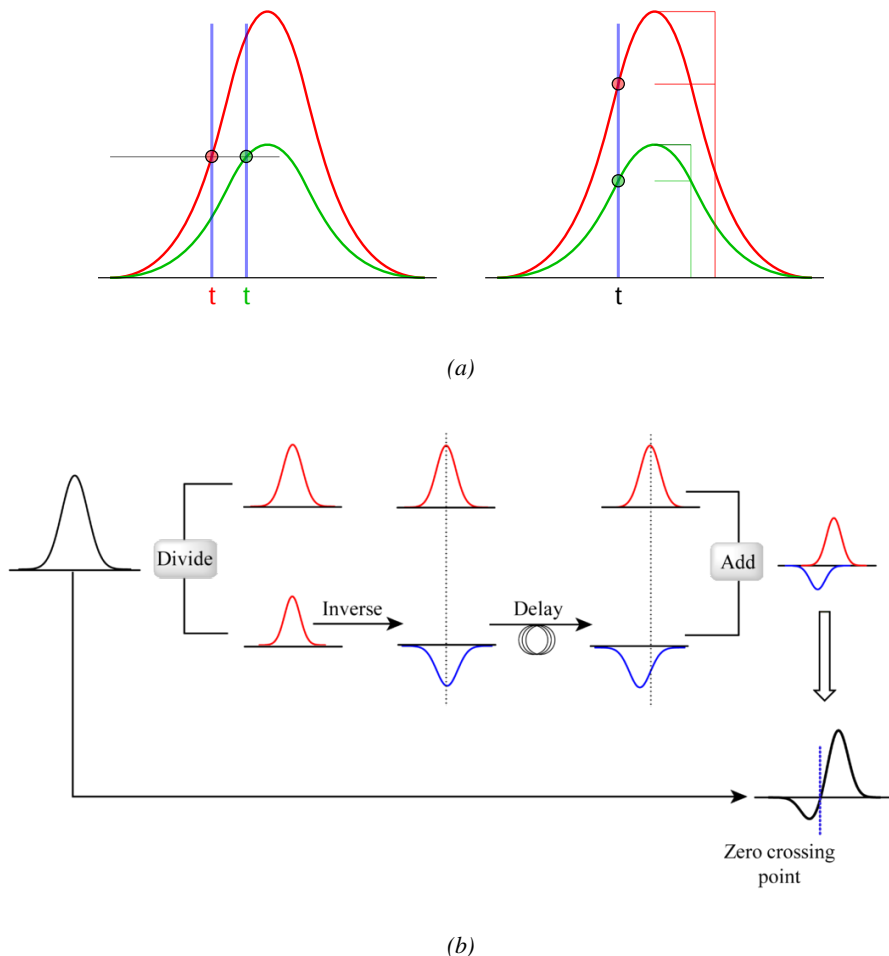


Figure 4.1: Signals from the RPC strips are shaped by the FEE described on Figure 4.1a. Output LVDS signals are then read-out by a TDC module connected to a computer or converted into NIM and sent to scalers. Figure 4.1b describes how these converted signals are put in coincidence with the trigger.



*Figure 4.2: Description of the principle of a CFD. A comparison of threshold triggering (left) and constant fraction triggering (right) is shown in Figure 4.2a. Constant fraction triggering is obtained thanks to zero-crossing technique as explained in Figure 4.2b. The signal arriving at the input of the CFD is split into three components. A first one is delayed and connected to the inverting input of a first comparator. A second component is connected to the noninverting input of another comparator along with a threshold value connected to the inverting input. Finally, the output of both comparators is fed through an AND gate.*

# 5

485

486

487

## Longevity studies and Consolidation of the present CMS RPC subsystem

488

### 5.1 Testing detectors under extreme conditions

489

The upgrade from LHC to HL-LHC will increase the peak luminosity from  $10^{34} \text{ cm}^{-2} \text{ s}^{-1}$  to reach  $5 \times 10^{34} \text{ cm}^{-2} \text{ s}^{-1}$ , increasing in the same way the total expected background to which the RPC system will be subjected to. Composed of low energy gammas and neutrons from  $p\text{-}p$  collisions, low momentum primary and secondary muons, puch-through hadrons from calorimeters, and particles produced in the interaction of the beams with collimators, the background will mostly affect the regions of CMS that are the closest to the beam line, i.e. the RPC detectors located in the endcaps.

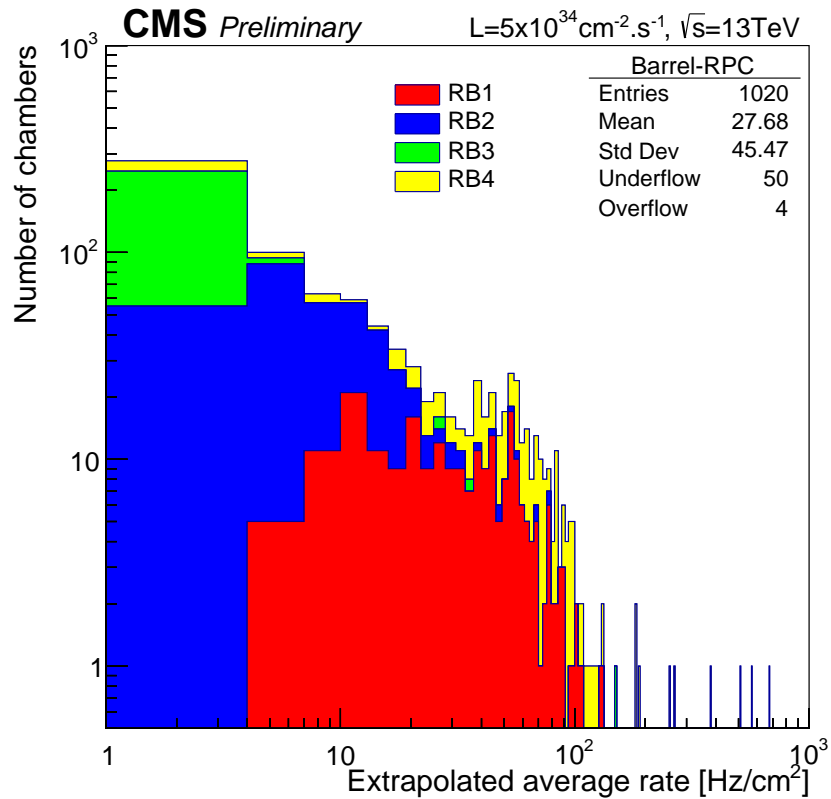
[To update.]

496

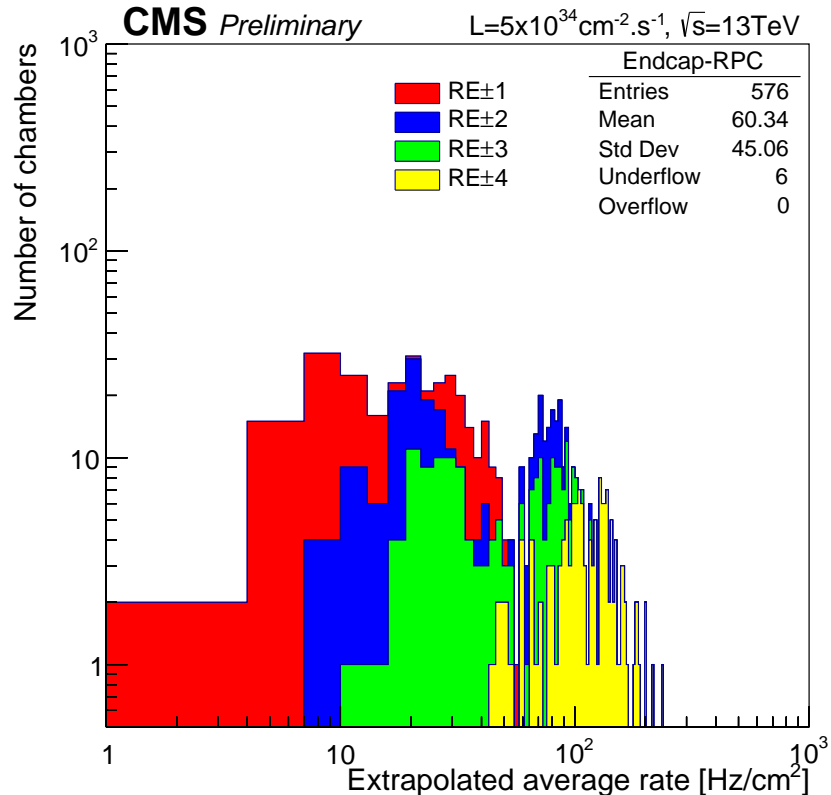
497

The 2016 data allowed to study the values of the background rate in all RPC system. In Figure 5.1, the distribution of the chamber background hit rate per unit area is shown at a luminosity of  $5 \times 10^{34} \text{ cm}^{-2} \cdot \text{s}^{-1}$  linearly extrapolating from data collected in 2016 [ref mentioning the linear dependency of rate vs lumi]. The maximum rate per unit area at HL-LHC conditions is expected to be of the order of  $600 \text{ Hz/cm}^2$  (including a safety factor 3). Nevertheless, Fluka simulations have conducted in order to understand the background at HL-LHC conditions. The comparison to the data has shown, in Figure 5.2, a discrepancy of a factor 2 even though the order of magnitude is consistent. [Understand mismatch.]

505



(a)



(b)

Figure 5.1: (5.1a) Extrapolation from 2016 data of single hit rate per unit area in the barrel region. (5.1b) Extrapolation from 2016 data of single hit rate per unit area in the endcap region.

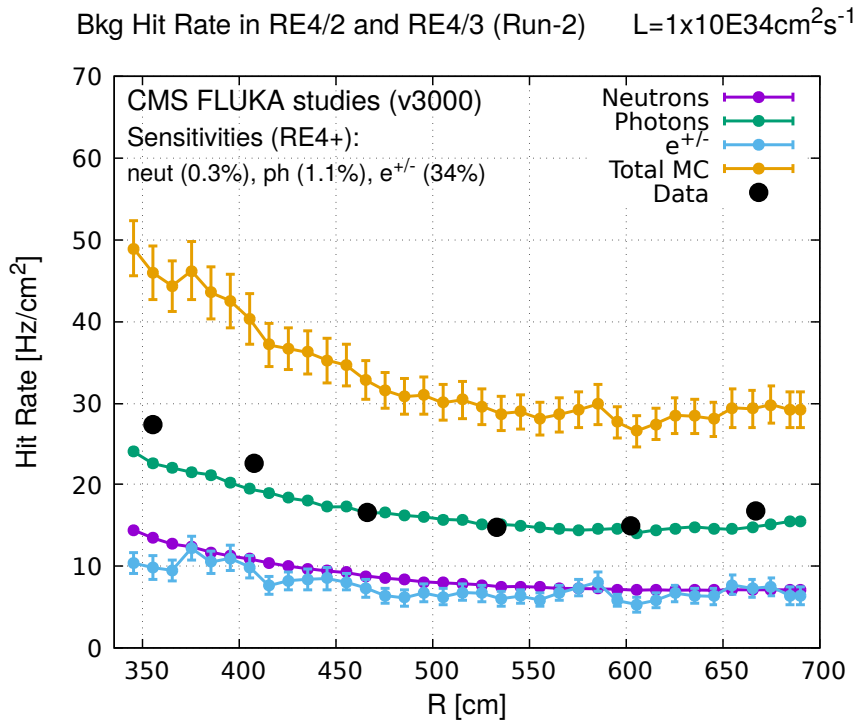


Figure 5.2: Background Fluka simulation compared to 2016 Data at  $L = 10^{34} \text{ cm}^{-2} \cdot \text{s}^{-1}$  in the fourth endcap disk region. A mismatch in between simulation and data can be observed. [\[To be understood.\]](#)

506 In the past, extensive long-term tests were carried out at several gamma and neutron facilities  
 507 certifying the detector performance. Both full size and small prototype RPCs have been irradiated  
 508 with photons up to an integrated charge of  $\sim 0.05 \text{ C/cm}^2$  and  $\sim 0.4 \text{ C/cm}^2$ , respectively [4, 5].  
 509 During Run-I, the RPC system provided stable operation and excellent performance and did not  
 510 show any aging effects for integrated charge of the order of  $0.01 \text{ C/cm}^2$ . Projections on currents  
 511 from 2016 Data, has allowed to determine that the total integrated charge, by the end of HL-LHC,  
 512 would be of the order of  $1 \text{ C/cm}^2$  (including a safety factor 3). [\[Corresponding figure needed.\]](#)

513

### 5.1.1 The Gamma Irradiation Facilities

#### 5.1.1.1 GIF

516 Located in the SPS West Area at the downstream end of the X5 test beam, the Gamma Irradiation  
 517 Facility (GIF) was a test area in which particle detectors were exposed to a particle beam in presence  
 518 of an adjustable gamma background [6]. Its goal was to reproduce background conditions these  
 519 detectors would suffer in their operating environment at LHC. GIF layout is shown in Figure 5.3.  
 520 Gamma photons are produced by a strong  $^{137}\text{Cs}$  source installed in the upstream part of the zone  
 521 inside a lead container. The source container includes a collimator, designed to irradiate a  $6 \times 6 \text{ m}^2$   
 522 area at 5 m maximum to the source. A thin lens-shaped lead filter helps providing with a uniform  
 523 outcoming flux in a vertical plane, orthogonal to the beam direction. The principal collimator hole  
 524 provides a pyramidal aperture of  $74^\circ \times 74^\circ$  solid angle and provides a photon flux in a pyramidal vol-

ume along the beam axis. The photon rate is controled by further lead filters allowing the maximum rate to be limited and to vary within a range of four orders of magnitude. Particle detectors under test are then placed within the pyramidal volume in front of the source, perpendicularly to the beam line in order to profit from the homogeneous photon flux. Adjusting the background flux of photons can then be done by using the filters and choosing the position of the detectors with respect to the source.

530

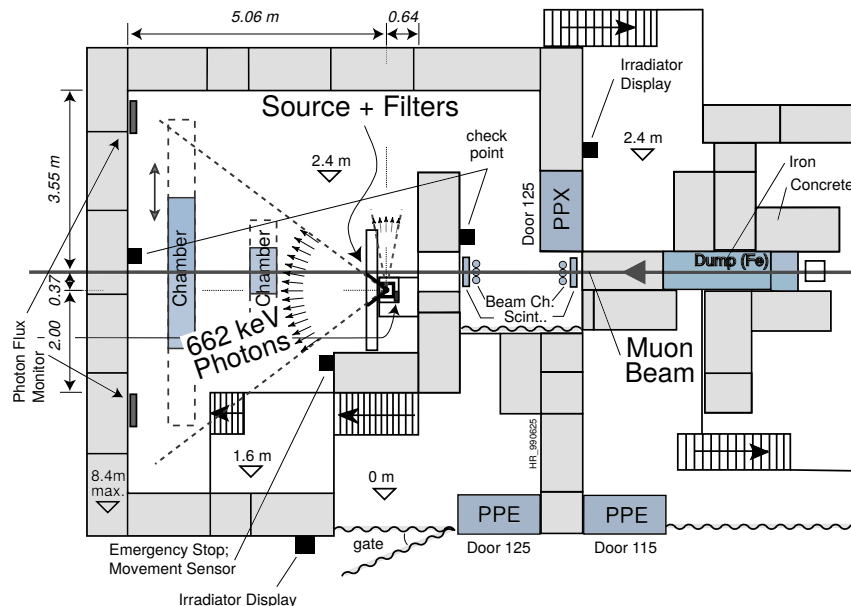


*Figure 5.3: Layout of the test beam zone called X5c GIF at CERN. Photons from the radioactive source produce a sustained high rate of random hits over the whole area. The zone is surrounded by 8 m high and 80 cm thick concrete walls. Access is possible through three entry points. Two access doors for personnel and one large gate for material. A crane allows installation of heavy equipment in the area.*

As described on Figure 5.4, the  $^{137}\text{Cs}$  source emits a 662 keV photon in 85% of the decays. An activity of 740 GBq was measured on the 5<sup>th</sup> March 1997. To estimate the strength of the flux in 2014, it is necessary to consider the nuclear decay through time assiciated to the Cesium source whose half-life is well known ( $t_{1/2} = (30.05 \pm 0.08)$  y). The GIF tests where done in between the 20<sup>th</sup> and the 31<sup>st</sup> of August 2014, i.e. at a time  $t = (17.47 \pm 0.02)$  y resulting in an attenuation of the activity from 740 GBq in 1997 to 494 GBq in 2014.

537

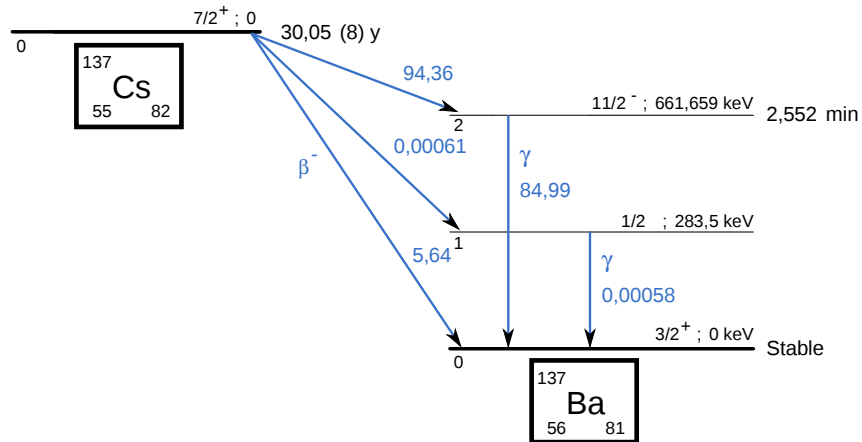


Figure 5.4:  $^{137}\text{Cs}$  decays by  $\beta^-$  emission to the ground state of  $^{137}\text{Ba}$  ( $BR = 5.64\%$ ) and via the 662 keV isomeric level of  $^{137}\text{Ba}$  ( $BR = 94.36\%$ ) whose half-life is 2.55 min.

### 5.1.1.2 GIF++

The new Gamma Irradiation Facility (GIF++), located in the SPS North Area at the downstream end of the H4 test beam, has replaced its predecessor during LS1 and has been operational since spring 2015 [7]. Like GIF, GIF++ features a  $^{137}\text{Cs}$  source of 662 keV gamma photons, their fluence being controlled with a set of filters of various attenuation factors. The source provides two separated large irradiation areas for testing several full-size muon detectors with continuous homogeneous irradiation, as presented in Figure 5.5.

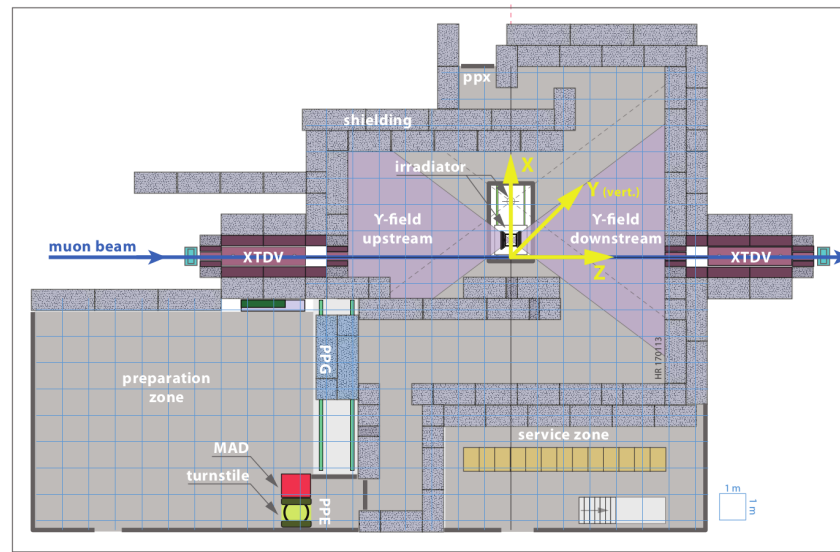
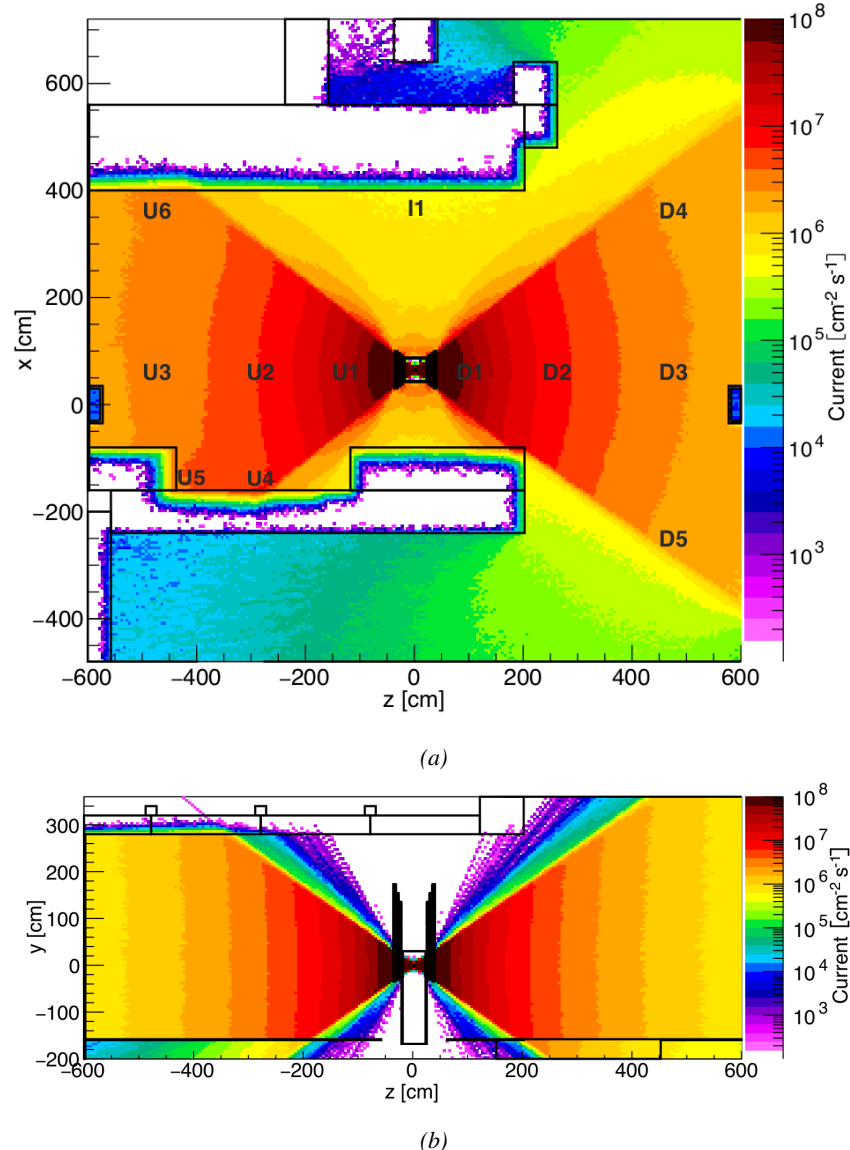


Figure 5.5: Floor plan of the GIF++ facility. When the facility downstream of the GIF++ takes electron beam, a beam pipe is installed along the beam line ( $z$ -axis). The irradiator can be displaced laterally (its center moves from  $x = 0.65$  m to  $2.15$  m), to increase the distance to the beam pipe.

546 The source activity was measured to be about 13.5 TBq in March 2016. The photon flux being  
 547 far greater than HL-LHC expectations, GIF++ provides an excellent facility for accelerated aging  
 548 tests of muon detectors.

549



*Figure 5.6: Simulated unattenuated current of photons in the xz plane (Figure 5.6a) and yz plane (Figure 5.6b) through the source at  $x = 0.65$  m and  $y = 0$  m. With angular correction filters, the current of 662 keV photons is made uniform in xy planes.*

550 The source is situated in the muon beam line with the muon beam being available a few times a  
 551 year. The H4 beam, composed of muons with a momentum of about 150 GeV/c, passes through the  
 552 GIF++ zone and is used to study the performance of the detectors. Its flux is of 104 particles/ $\text{s cm}^2$

553 focused in an area similar to  $10 \times 10 \text{ cm}^2$ . Therefore, with properly adjusted filters, one can imitate  
 554 the HL-LHC background and study the performance of muon detectors with their trigger/readout  
 555 electronics in HL-LHC environment.

556

## 557 5.2 Preliminary tests at GIF

### 558 5.2.1 Resistive Plate Chamber test setup

559 During summer 2014, preliminary tests have been conducted in the GIF area on a newly produced  
 560 RE4/2 chamber labelled RE-4-2-BARC-161. This chamber has been placed into a trolley covered  
 561 with a tent. The position of the RPC inside the tent and of the tent related to the source is described  
 562 in Figure 5.7. To test this CMS RPC, three different absorber settings were used. First of all,  
 563 measurements were done with fully opened source. Then, to complete this preliminary study, the  
 564 gamma flux has been attenuated from a factor 2 and a factor 5. The expected gamma flux at the level  
 565 of our detector will be discussed in subsection ??.

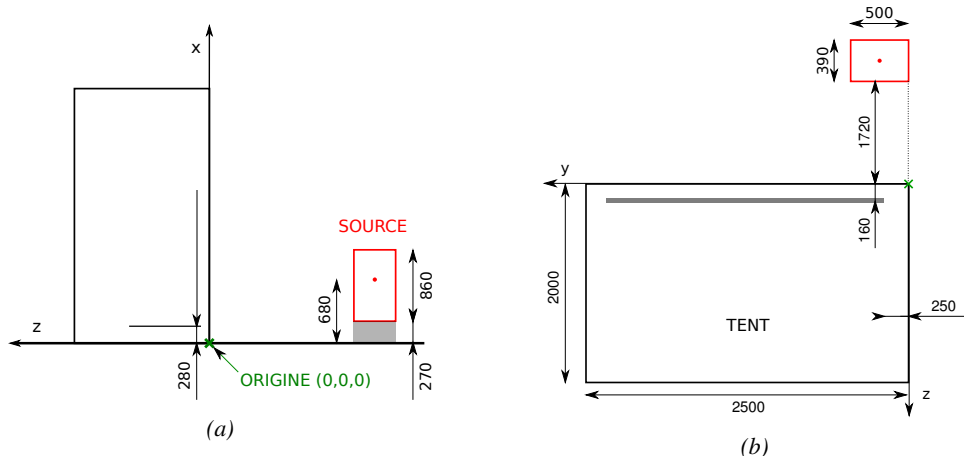
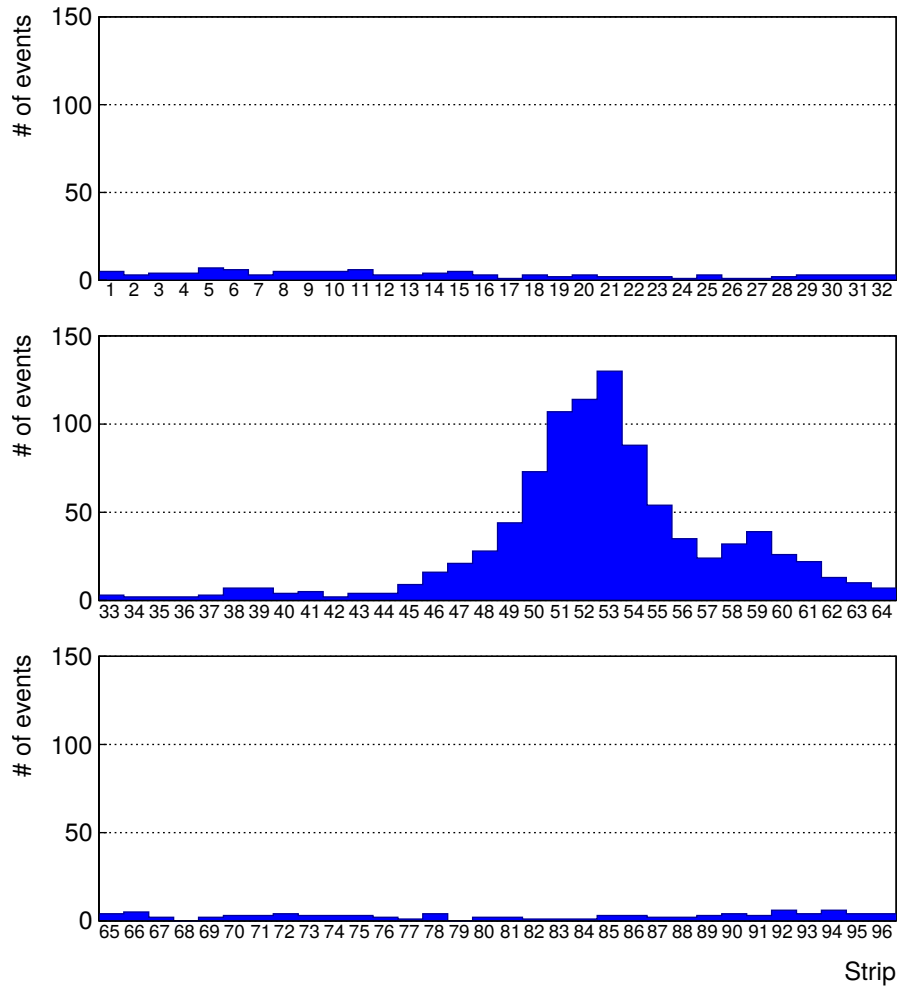


Figure 5.7: Description of the RPC setup. Dimensions are given in mm. A tent containing RPCs is placed at 1720 mm from the source container. The source is situated in the center of the container. RE-4-2-BARC-161 chamber is 160 mm inside the tent. This way, the distance between the source and the chambers plan is 2060 mm. Figure 5.7a provides a side view of the setup in the xz plane while Figure 5.7b shows a top view in the yz plane.



*Figure 5.8: RE-4-2-BARC-161 chamber is inside the tent as described in Figure 5.7. In the top right, the two scintillators used as trigger can be seen. This trigger system has an inclination of 10° relative to horizontal and is placed above half-partition B2 of the RPCs. PMT electronics are shielded thanks to lead blocks placed in order to protect them without stopping photons from going through the scintillators and the chamber.*

566 At the time of the tests, the beam not being operational anymore, a trigger composed of 2  
567 plastic scintillators has been placed in front of the setup with an inclination of 10 deg with respect to  
568 the detector plane in order to look at cosmic muons. Using this particular trigger layout, shown on  
569 Figure 5.8, leads to a cosmic muon hit distribution into the chamber similar to the one in Figure 5.9.  
570 Measured without gamma irradiation, two peaks can be seen on the profil of partition B, centered  
571 on strips 52 and 59. Section ?? will help us understand that these two peaks are due respectively to  
572 forward and backward coming cosmic particles where forward coming particles are first detected by  
573 the scintillators and then the RPC while the backward coming muons are first detected in the RPC.



*Figure 5.9: Hit distributions over all 3 partitions of RE-4-2-BARC-161 chamber is showed on these plots. Top, middle and bottom figures respectively correspond to partitions A, B, and C. These plots show that some events still occur in other half-partitions than B2, which corresponds to strips 49 to 64, in front of which the trigger is placed, contributing to the inefficiency of detection of cosmic muons. In the case of partitions A and C, the very low amount of data can be interpreted as noise. On the other hand, it is clear that a little portion of muons reach the half-partition B1, corresponding to strips 33 to 48.*

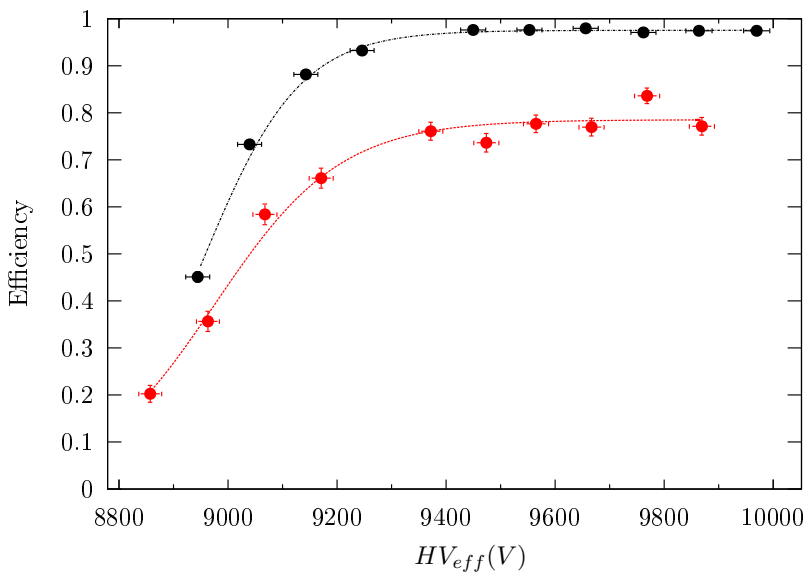
574    **5.2.2 Data Acquisition**

575    **5.2.3 Geometrical acceptance of the setup layout to cosmic muons**

576    In order to profit from a constant gamma irradiation, the detectors inside of the GIF bunker need  
 577    to be placed in a plane orthogonal to the beam line. The muon beam that used to be available was  
 578    meant to test the performance of detectors under test. This beam not being active anymore, another  
 579    solution to test detector performance had to be used. Thus, it has been decided to use cosmic muons  
 580    detected through a telescope composed of two scintillators. Lead blocks were used as shielding to

581 protect the photomultipliers from gammas as can be seen from Figure 5.8.

582 An inclination has been given to the cosmic telescope to maximize the muon flux. A good com-  
 583 promise had to be found between good enough muon flux and narrow enough hit distribution to  
 584 be sure to contain all the events into only one half partitions as required from the limited available  
 585 readout hardware. Nevertheless, a consequence of the misplaced trigger, that can be seen as a loss  
 586 of events in half-partition B1 in Figure 5.9, is an inefficiency. Nevertheless, the inefficiency of ap-  
 587 proximately 20 % highlighted in Figure 5.10 by comparing the performance of chamber BARC-161  
 588 in 904 and at GIF without irradiation seems too important to be explained only by the geometri-  
 589 cal acceptance of the setup itself. Simulations have been conducted to show how the setup brings  
 590 inefficiency.



591 *Figure 5.10: Results are derived from data taken on half-partition B2 only. On the 18<sup>th</sup> of June 2014, data  
 592 has been taken on chamber RE-2-BARC-161 at building 904 (Prevessin Site) with cosmic muons providing us a  
 593 reference efficiency plateau of  $(97.54 \pm 0.15)\%$  represented by a black curve. A similar measurement has been  
 594 done at GIF on the 21<sup>st</sup> of July with the same chamber giving a plateau of  $(78.52 \pm 0.94)\%$  represented by a  
 595 red curve.*

### 596 5.2.3.1 Description of the simulation layout

597 The layout of GIF setup has been reproduced and incorporated into a Monte Carlo (MC) simulation  
 598 to study the influence of the disposition of the telescope on the final distribution measured by the  
 599 RPC. A 3D view of the simulated layout is given into Figure 5.11. Muons are generated randomly  
 600 in a horizontal plane located at a height corresponding to the lowest point of the PMTs. This way,  
 601 the needed size of the plane in order to simulate events happening at very big azimuthal angles (i.e.  
 $\theta \approx \pi$ ) can be kept relatively small. The muon flux is designed to follow the usual  $\cos^2\theta$  distribution  
 602 for cosmic particle. The goal of the simulation is to look at muons that pass through the muon  
 603 telescope composed of the two scintillators and define their distribution onto the RPC plane. During  
 604 the reconstruction, the RPC plane is then divided into its strips and each muon track is assigned to a  
 605 strip.

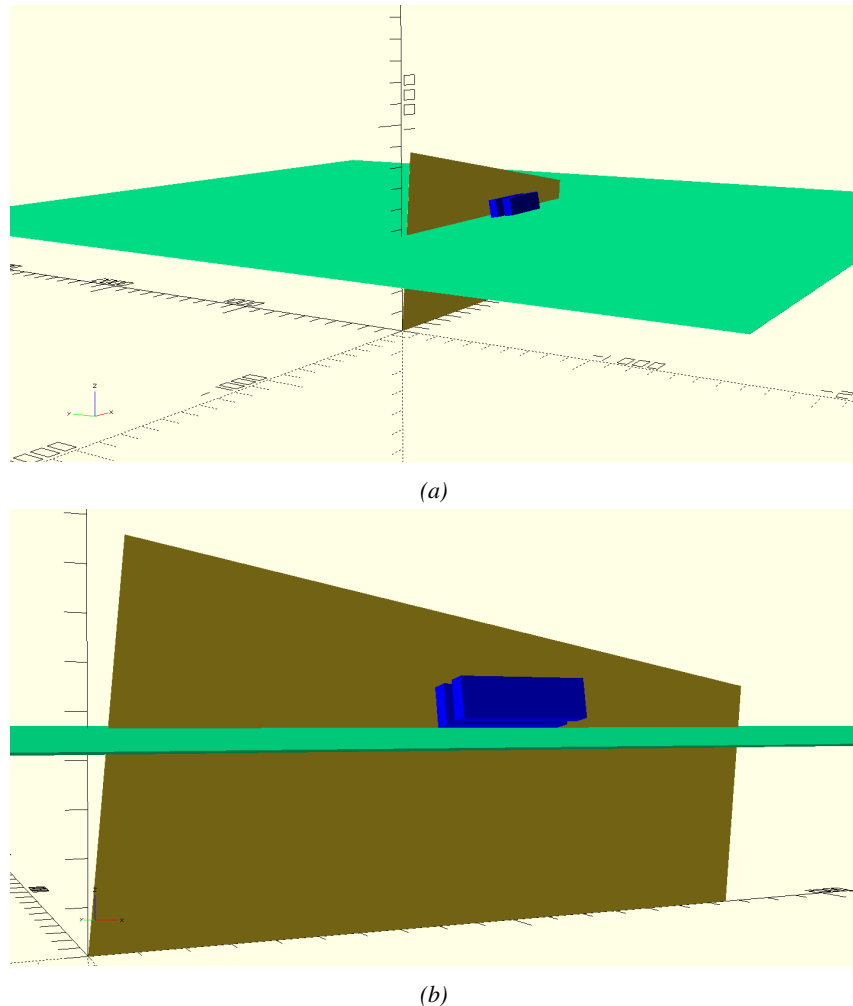


*Figure 5.11: Representation of the layout used for the simulations of the test setup. The RPC is represented as a yellow trapezoid while the two scintillators as blue cuboids looking at the sky. A green plane corresponds to the muon generation plane within the simulation. Figure 5.7a shows a global view of the simulated setup. Figure 5.7b shows a zoomed view that allows to see the 2 scintillators as well as the full RPC plane.*

602 In order to further refine the quality of the simulation and understand deeper the results the  
 603 dependance of the distribution has been studied for a range of telescope inclinations. Moreover,  
 604 the threshold applied on the PMT signals has been included into the simulation in the form of a  
 605 cut. In the approximation of uniform scintillators, it has been considered that the threshold can be  
 606 understood as the minimum distance particles need to travel through the scintillating material to give  
 607 a strong enough signal. Particles that travel a distance smaller than the set "threshold" are thus not  
 608 detected by the telescope and cannot trigger the data taking. Finally, the FEE threshold also has  
 609 been considered in a similar way. The mean momentum of horizontal cosmic rays is higher than  
 610 those of vertical ones but the stopping power of matter for momenta ranging from 1 GeV to 1 TeV  
 611 stays comparable. It is then possible to assume that the mean number of primary  $e^-/ion$  pairs per  
 612 unit length will stay similar and thus, depending on the applied discriminator threshold, muons with

613 the shortest path through the gas volume will deposit less charge and induce a smaller signal on the  
 614 pick-up strips that could eventually not be detected. These two thresholds also restrain the overall  
 615 geometrical acceptance of the system.

616 **5.2.3.2 Simulation procedure**

617 The simulation software has been designed using C++ and the output data is saved into ROOT  
 618 histograms. Simulations start for a threshold  $T_{scint}$  varying in a range from 0 to 45 mm in steps  
 619 of 5 mm, where  $T_{scint} = 0$  mm corresponds to the case where there isn't any threshold apply on  
 620 the input signal while  $T_{scint} = 45$  mm, which is the scintillator thickness, is the case where muons  
 621 cannot arrive orthogonally onto the scintillator surface. For a given  $T_{scint}$ , a set of RPC thresholds  
 622 are considered. The RPC threshold,  $T_{RPC}$  varies from 2 mm, the thickness of the gas volume, to  
 623 3 mm in steps of 0.25 mm. For each  $(T_{scint}; T_{RPC})$  pair,  $N_\mu = 10^8$  muons are randomly generated  
 624 inside the muon plane described in the previous paragraph with an azimuthal angle  $\theta$  chosen to follow  
 625 a  $\cos^2\theta$  distribution.

626 Planes are associated to each surface of the scintillators. Knowing muon position into the muon  
 627 plane and its direction allows us, by assuming that muons travel in a straight line, to compute the  
 628 intersection of the muon track with these planes. Applying conditions to the limits of the surfaces  
 629 of the scintillator faces then gives us an answer to whether or not the muon passed through the  
 630 scintillators. In the case the muon has indeed passed through the telescope, the path through each  
 631 scintillator is computed and muons whose path was shorter than  $T_{scint}$  are rejected and are thus  
 632 considered as having not interacted with the setup.

633 On the contrary, if the muon is labeled as good, its position within the RPC plane is computed  
 634 and the corresponding strip, determined by geometrical tests in the case the distance through the  
 635 gas volume was enough not to be rejected because of  $T_{RPC}$ , gets a hit and several histograms  
 636 are filled in order to keep track of the generation point on the muon plane, the intersection points  
 637 of the reconstructed muons within the telescope, or on the RPC plane, the path traveled through  
 638 each individual scintillator or the gas volume, as well as other histograms. Moreover, muons fill  
 639 different histograms whether they are forward or backward coming muons. They are discriminated  
 640 according to their direction components. When a muon is generated, an  $(x, y, z)$  position is assigned  
 641 into the muon plane as well as a  $(\theta; \phi)$  pair that gives us the direction it's coming from. This way,  
 642 muons satisfying the condition  $0 \leq \phi < \pi$  are designated as backward coming muons while muons  
 643 satisfying  $\pi \leq \phi < 2\pi$  as forward coming muons.

644 This simulation is then repeated for different telescope inclinations ranging in between 4 and  $20^\circ$   
 645 and varying in steps of  $2^\circ$ . Due to this inclination and to the vertical position of the detector under  
 646 test, the muon distribution reconstructed in the detector plane is asymmetrical. The choice as been  
 647 made to chose a skew distribution formula to fit the data built as the multiplication of gaussian and  
 648 sigmoidal curves together. A typical gaussian formula is given as 5.1 and has three free parameters  
 649 as  $A_g$ , its amplitude,  $\bar{x}$ , its mean value and  $\sigma$ , its root mean square. Sigmoidal curves as given by  
 650 formula 5.2 are functions converging to 0 and  $A_s$  as  $x$  diverges. The inflection point is given as  $x_i$   
 651 and  $\lambda$  is proportional to the slope at  $x = x_i$ . In the limit where  $\lambda \rightarrow \infty$ , the sigmoid becomes a  
 652 step function.

$$g(x) = A_g e^{-\frac{(x-\bar{x})^2}{2\sigma^2}} \quad (5.1)$$

$$s(x) = \frac{A_s}{1 + e^{-\lambda(x-x_i)}} \quad (5.2)$$

653 Finally, a possible representation of a skew distribution is given by formula 5.3 and is the product  
 654 of 5.1 and 5.2. Naturally, here  $A_{sk} = A_g \times A_s$  and represents the theoretical maximum in the limit  
 655 where the skew tends to a gaussian function.

$$sk(x) = g(x) \times s(x) = A_{sk} \frac{e^{\frac{-(x-\bar{x})^2}{2\sigma^2}}}{1 + e^{-\lambda(x-x_i)}} \quad (5.3)$$

656 **5.2.3.3 Results**

657 **Influence of  $T_{scint}$  on the muon distribution**

658 **Influence of  $T_{RPC}$  on the muon distribution**

659 **Influence of the telescope inclination on the muon distribution**

660 **Comparison to data taken at GIF without irradiation**

661 **5.2.4 Photon flux at GIF**

662 **5.2.4.1 Expectations from simulations**

663 In order to understand and evaluate the  $\gamma$  flux in the GIF area, simulations had been conducted in  
 664 1999 and published by S. Agosteo et al [6]. Table 5.1 presented in this article gives us the  $\gamma$  flux  
 665 for different distances  $D$  to the source. This simulation was done using GEANT and a Monte Carlo  
 666 N-Particle (MCNP) transport code, and the flux  $F$  is given in number of  $\gamma$  per unit area and unit time  
 667 along with the estimated error from these packages expressed in %.

| Nominal<br>ABS | Photon flux $F$ [ $s^{-1}cm^{-2}$ ] |                             |                             |                             |
|----------------|-------------------------------------|-----------------------------|-----------------------------|-----------------------------|
|                | at $D = 50$ cm                      | at $D = 155$ cm             | at $D = 300$ cm             | at $D = 400$ cm             |
| 1              | $0.12 \cdot 10^8 \pm 0.2\%$         | $0.14 \cdot 10^7 \pm 0.5\%$ | $0.45 \cdot 10^6 \pm 0.5\%$ | $0.28 \cdot 10^6 \pm 0.5\%$ |
| 2              | $0.68 \cdot 10^7 \pm 0.3\%$         | $0.80 \cdot 10^6 \pm 0.8\%$ | $0.25 \cdot 10^6 \pm 0.8\%$ | $0.16 \cdot 10^6 \pm 0.6\%$ |
| 5              | $0.31 \cdot 10^7 \pm 0.4\%$         | $0.36 \cdot 10^6 \pm 1.2\%$ | $0.11 \cdot 10^6 \pm 1.2\%$ | $0.70 \cdot 10^5 \pm 0.9\%$ |

Table 5.1: Total photon flux ( $E\gamma \leq 662$  keV) with statistical error predicted considering a  $^{137}Cs$  activity of 740 GBq at different values of the distance  $D$  to the source along the  $x$ -axis of irradiation field [6].

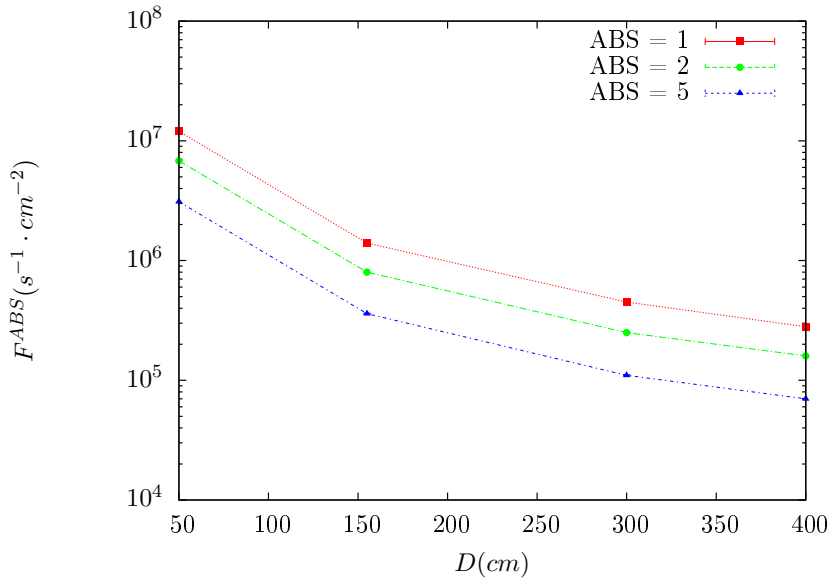


Figure 5.12:  $\gamma$  flux  $F(D)$  is plot using values from table 5.1. As expected, the plot shows similar attenuation behaviours with increasing distance for each absorption factors.

The simulation doesn't directly provides us with an estimated flux at the level of our RPC. First of all, it is needed to extract the value of the flux from the available data contained in the original paper and then to estimate the flux in 2014 at the time the experimentation took place. Figure 5.12 that contains the data from Table 5.1. In the case of a pointlike source emitting isotropic and homogeneous gamma radiations, the gamma flux  $F$  at a distance  $D$  to the source with respect to a reference point situated at  $D_0$  where a known flux  $F_0$  is measured will be expressed like in Equation 5.4, assuming that the flux decreases as  $1/D^2$ , where  $c$  is a fitting factor.

$$F^{ABS} = F_0^{ABS} \times \left( \frac{cD_0}{D} \right)^2 \quad (5.4)$$

By rewriting Equation 5.4, it comes that :

$$c = \frac{D}{D_0} \sqrt{\frac{F^{ABS}}{F_0^{ABS}}} \quad (5.5)$$

$$\Delta c = \frac{c}{2} \left( \frac{\Delta F^{ABS}}{F^{ABS}} + \frac{\Delta F_0^{ABS}}{F_0^{ABS}} \right) \quad (5.6)$$

Finally, using Equation 5.5 and the data in Table 5.1 with  $D_0 = 50$  cm as reference point, we can build Table 5.2. It is interesting to note that  $c$  for each value of  $D$  doesn't depend on the absorption factor.

| Nominal<br>ABS | Correction factor $c$ |                    |                    |
|----------------|-----------------------|--------------------|--------------------|
|                | at $D = 155$ cm       | at $D = 300$ cm    | at $D = 400$ cm    |
| 1              | $1.059 \pm 0.70\%$    | $1.162 \pm 0.70\%$ | $1.222 \pm 0.70\%$ |
| 2              | $1.063 \pm 1.10\%$    | $1.150 \pm 1.10\%$ | $1.227 \pm 0.90\%$ |
| 5              | $1.056 \pm 1.60\%$    | $1.130 \pm 1.60\%$ | $1.202 \pm 1.30\%$ |

Table 5.2: Correction factor  $c$  is computed thanks to formulae 5.5 taking as reference  $D_0 = 50$  cm and the associated flux  $F_0^{ABS}$  for each absorption factor available in table 5.1.

679 For the range of  $D/D_0$  values available, it is possible to use a simple linear fit to get the evolution  
 680 of  $c$ . The linear fit will then use only 2 free parameters,  $a$  and  $b$ , as written in Equation 5.7. This gives  
 681 us the results showed in Figure 5.13. Figure 5.13b confirms that using only a linear fit to extract  $c$  is  
 682 enough as the evolution of the rate that can be obtained superimposes well on the simulation points.

$$c \left( \frac{D}{D_0} \right) = a \frac{D}{D_0} + b \quad (5.7)$$

$$F^{ABS} = F_0^{ABS} \left( a + \frac{bD_0}{D} \right)^2 \quad (5.8)$$

$$\Delta F^{ABS} = F^{ABS} \left[ \frac{\Delta F_0^{ABS}}{F_0^{ABS}} + 2 \frac{\Delta a + \Delta b \frac{D_0}{D}}{a + \frac{bD_0}{D}} \right] \quad (5.9)$$

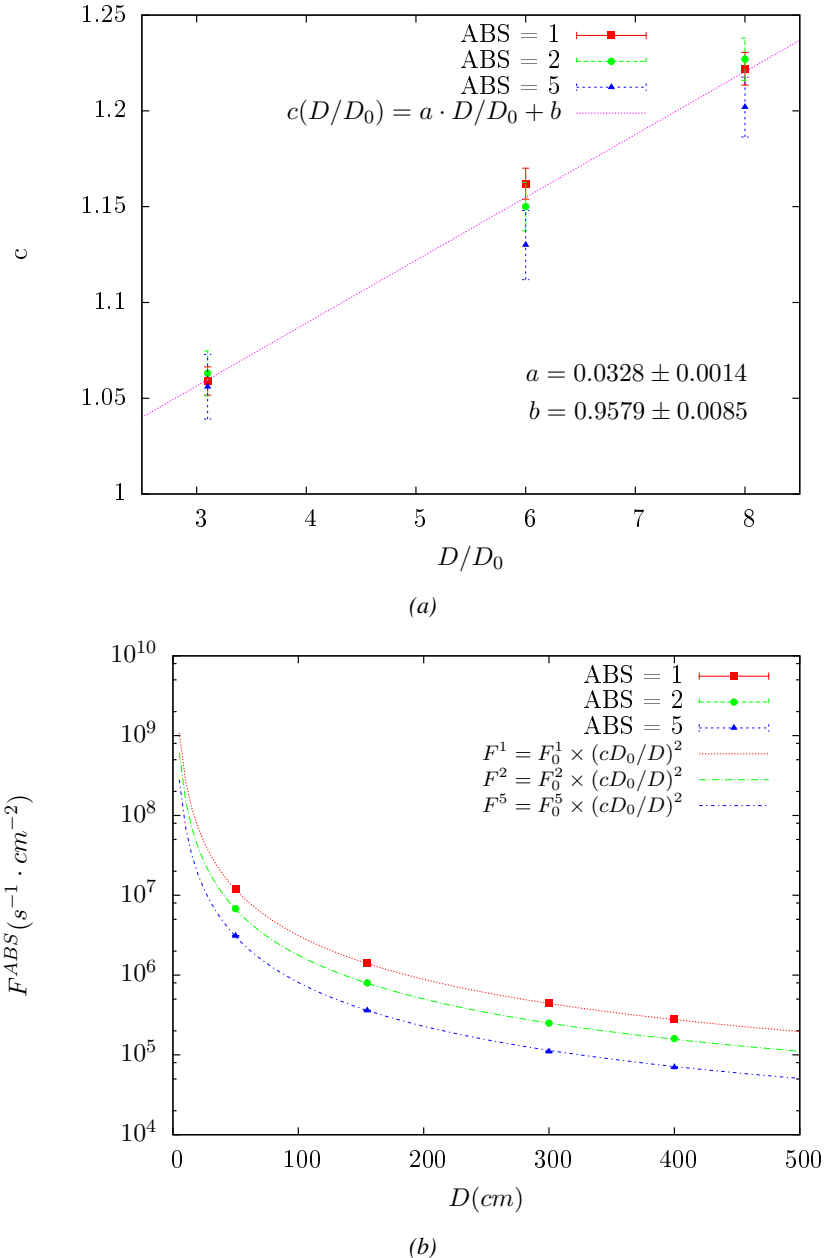


Figure 5.13: Figure 5.13a shows the linear approximation fit done via formulae 5.7 on data from table 5.2. Figure 5.13b shows a comparison of this model with the simulated flux using  $a$  and  $b$  given in figure 5.13a in formulae 5.4 and the reference value  $D_0 = 50\text{cm}$  and the associated flux for each absorption factor  $F_0^{ABS}$  from table 5.1

In the case of the 2014 GIF tests, the RPC plane is located at a distance  $D = 206\text{ cm}$  to the source. Moreover, to estimate the strength of the flux in 2014, it is necessary to consider the nuclear decay through time associated to the Cesium source whose half-life is well known ( $t_{1/2} = (30.05 \pm 0.08)\text{ y}$ ). The very first source activity measurement has been done on the 5<sup>th</sup> of March 1997 while the GIF

687 tests where done in between the 20<sup>th</sup> and the 31<sup>st</sup> of August 2014, i.e. at a time  $t = (17.47 \pm 0.02)$  y  
 688 resulting in an attenuation of the activity from 740 GBq in 1997 to 494 GBq in 2014. All the needed  
 689 information to extrapolate the flux through our detector in 2014 has now been assembled, leading  
 690 to the Table 5.3. It is interesting to note that for a common RPC sensitivity to  $\gamma$  of  $2 \cdot 10^{-3}$ , the  
 691 order of magnitude of the estimated hit rate per unit area is of the order of the kHz for the fully  
 692 opened source. Moreover, taking profit of the two working absorbers, it will be possible to scan  
 693 background rates at 0 Hz,  $\sim 300$  Hz as well as  $\sim 600$  Hz. Without source, a good estimate of the  
 694 intrinsic performance will be available. Then at 300 Hz, the goal will be to show that the detectors  
 695 fulfill the performance certification of CMS RPCs. Then a first idea of the performance of the  
 696 detectors at higher background will be provided with absorption factors 2 ( $\sim 600$  Hz) and 1 (no  
 697 absorption). *[Here I will also put a reference to the plot showing the estimated background rate at  
 698 the level of RE3/1 in the case of HL-LHC but this one being in another chapter, I will do it later.]*

| Nominal ABS | Photon flux $F$ [ $s^{-1}cm^{-2}$ ] |                             |                             | Hit rate/unit area [ $Hz cm^{-2}$ ]<br>at $D^{2014} = 206$ cm |
|-------------|-------------------------------------|-----------------------------|-----------------------------|---|
|             | at $D_0^{1997} = 50$ cm             | at $D_0^{1997} = 206$ cm    | at $D^{2014} = 206$ cm      |   |
| 1           | $0.12 \cdot 10^8 \pm 0.2\%$         | $0.84 \cdot 10^6 \pm 0.3\%$ | $0.56 \cdot 10^6 \pm 0.3\%$ | $1129 \pm 32$   |
| 2           | $0.68 \cdot 10^7 \pm 0.3\%$         | $0.48 \cdot 10^6 \pm 0.3\%$ | $0.32 \cdot 10^6 \pm 0.3\%$ | $640 \pm 19$  |
| 5           | $0.31 \cdot 10^7 \pm 0.4\%$         | $0.22 \cdot 10^6 \pm 0.3\%$ | $0.15 \cdot 10^6 \pm 0.3\%$ | $292 \pm 9$   |

Table 5.3: The data at  $D_0$  in 1997 is taken from [6]. In a second step, using Equations 5.8 and 5.9, the flux at  $D$  can be estimated in 1997. Then, taking into account the attenuation of the source activity, the flux at  $D$  can be estimated at the time of the tests in GIF in 2014. Finally, assuming a sensitivity of the RPC to  $\gamma$   $s = 2 \cdot 10^{-3}$ , an estimation of the hit rate per unit area is obtained.

<sup>699</sup> **5.2.4.2 Dose measurements**

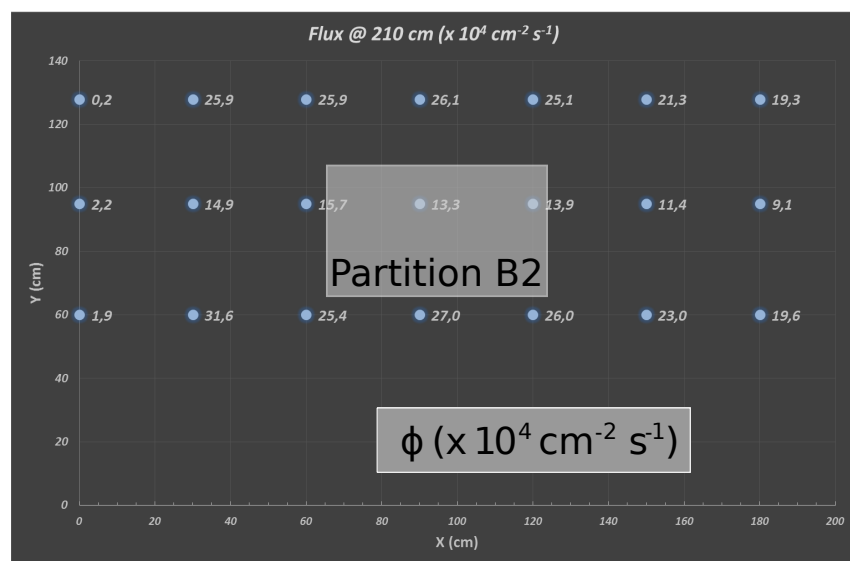


Figure 5.14: Dose measurements has been done in a plane corresponding to the tents front side. This plan is 1900 mm away from the source. As explained in the first chapter, a lens-shaped lead filter provides a uniform photon flux in the vertical plan orthogonal to the beam direction. If the second line of measured fluxes is not taken into account because of lower values due to experimental equipments in the way between the source and the tent, the uniformity of the flux is well showed by the results.

<sup>700</sup> **5.2.5 Results and discussions**

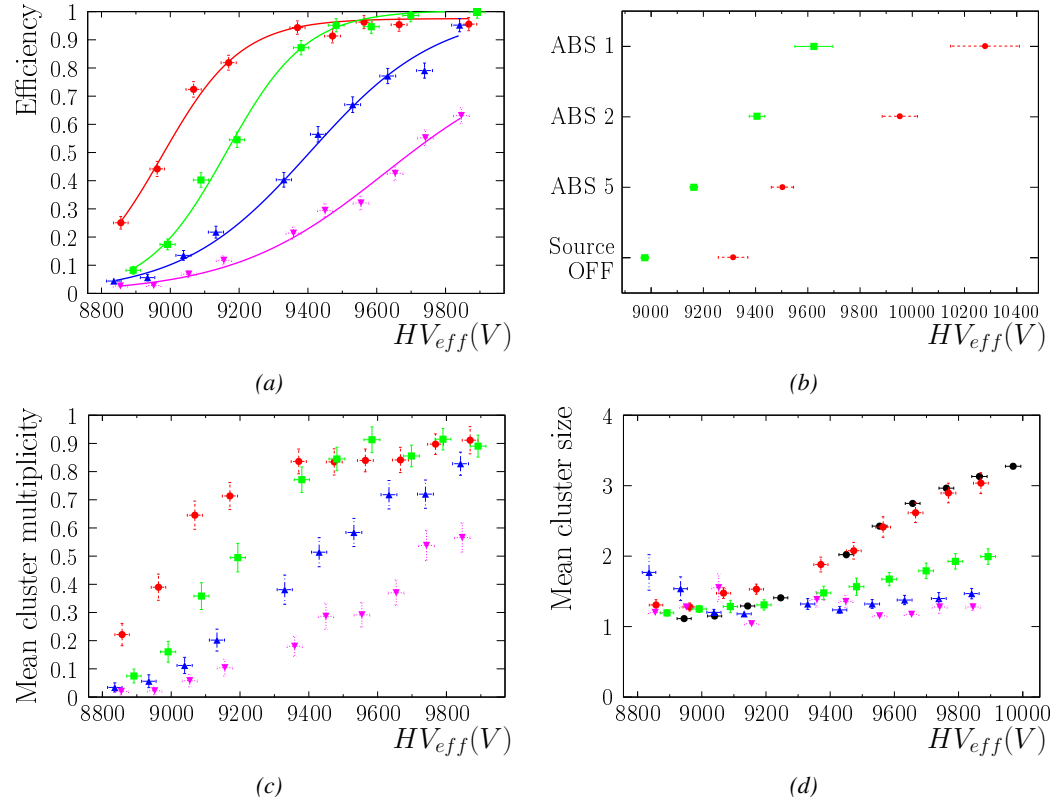


Figure 5.15

<sup>701</sup> **5.3 Longevity tests at GIF++**

<sup>702</sup> Longevity studies imply a monitoring of the performance of the detectors probed using a high inten-  
<sup>703</sup> sity muon beam in a irradiated environment by periodically measuring their rate capability, the dark  
<sup>704</sup> current running through them and the bulk resistivity of the Bakelite composing their electrodes.  
<sup>705</sup> GIF++, with its very intense  $^{137}\text{Cs}$  source, provides the perfect environment to perform such kind  
<sup>706</sup> of tests. Assuming a maximum acceleration factor of 3, it is expected to accumulate the equivalent  
<sup>707</sup> charge in 1.7 years.

<sup>708</sup> As the maximum background is found in the endcap, the choice naturally was made to focus the  
<sup>709</sup> GIF++ longevity studies on endcap chambers. Most of the RPC system was installed in 2007. Nev-  
<sup>710</sup> ertheless, the large chambers in the fourth endcap (RE4/2 and RE4/3) have been installed during  
<sup>711</sup> LS1 in 2014. The Bakelite of these two different productions having different properties, four spare  
<sup>712</sup> chambers of the present system were selected, two RE2,3/2 spares and two RE4/2 spares. Having  
<sup>713</sup> two chambers of each type allows to always keep one of them non irradiated as reference, the per-  
<sup>714</sup> formance evolution of the irradiated chamber being then compared through time to the performance  
<sup>715</sup> of the non irradiated one.

<sup>716</sup> The performance of the detectors under different level of irradiation is measured periodically dur-  
<sup>717</sup> ing dedicated test beam periods using the H4 muon beam. In between these test beam periods, the  
<sup>718</sup> two RE2,3/2 and RE4/2 chambers selected for this study are irradiated by the  $^{137}\text{Cs}$  source in order  
<sup>719</sup> to accumulate charge and the gamma background is monitored, as well as the currents. The two  
<sup>720</sup> remaining chambers are kept non-irradiated as reference detectors. Due to the limited gas flow in  
<sup>721</sup> GIF++, the RE4 chamber remained non-irradiated until end of November 2016 where a new mass  
<sup>722</sup> flow controller has been installed allowing for bigger volumes of gas to flow in the system.

<sup>723</sup> Figures 5.16 and 5.17 give us for different test beam periods, and thus for increasing integrated  
<sup>724</sup> charge through time, a comparison of the maximum efficiency, obtained using a sigmoid-like func-  
<sup>725</sup> tion, and of the working point of both irradiated and non irradiated chambers [8]. No aging is yet to  
<sup>726</sup> see from this data, the shifts in  $\gamma$  rate per unit area in between irradiated and non irradiated detec-  
<sup>727</sup> tors and RE2 and RE4 types being easily explained by a difference of sensitivity due to the various  
<sup>728</sup> Bakelite resistivities of the HPL electrodes used for the electrode production.

<sup>729</sup> Collecting performance data at each test beam period allows us to extrapolate the maximum effi-  
<sup>730</sup> ciency for a background hit rate of  $300\text{ Hz}/\text{cm}^2$  corresponding to the expected HL-LHC conditions.  
<sup>731</sup> Aging effects could emerge from a loss of efficiency with increasing integrated charge over time,  
<sup>732</sup> thus Figure 5.18 helps us understand such degradation of the performance of irradiated detectors in  
<sup>733</sup> comparison with non irradiated ones. The final answer for an eventual loss of efficiency is given in  
<sup>734</sup> Figure 5.19 by comparing for both irradiated and non irradiated detectors the efficiency sigmoids  
<sup>735</sup> before and after the longevity study. Moreover, to complete the performance information, the Bake-  
<sup>736</sup> lite resistivity is regularly measured thanks to  $Ag$  scans (Figure 5.20) and the noise rate is monitored  
<sup>737</sup> weekly during irradiation periods (Figure 5.21). At the end of 2016, no signs of aging were observed  
<sup>738</sup> and further investigation is needed to get closer to the final integrated charge requirements proposed  
<sup>739</sup> for the longevity study of the present CMS RPC sub-system.

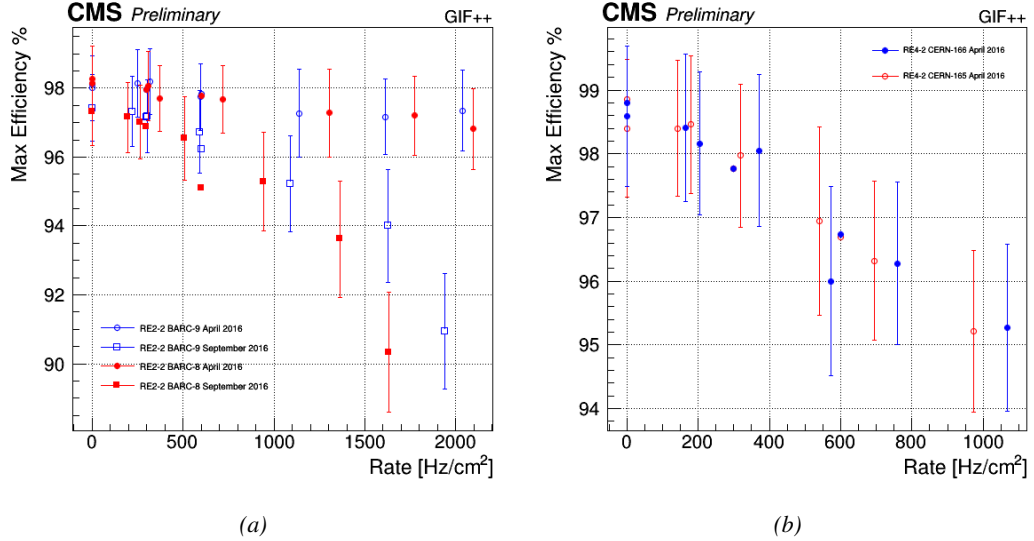


Figure 5.16: Evolution of the maximum efficiency for RE2 (5.16a) and RE4 (5.16b) chambers with increasing extrapolated  $\gamma$  rate per unit area at working point. Both irradiated (blue) and non irradiated (red) chambers are shown.

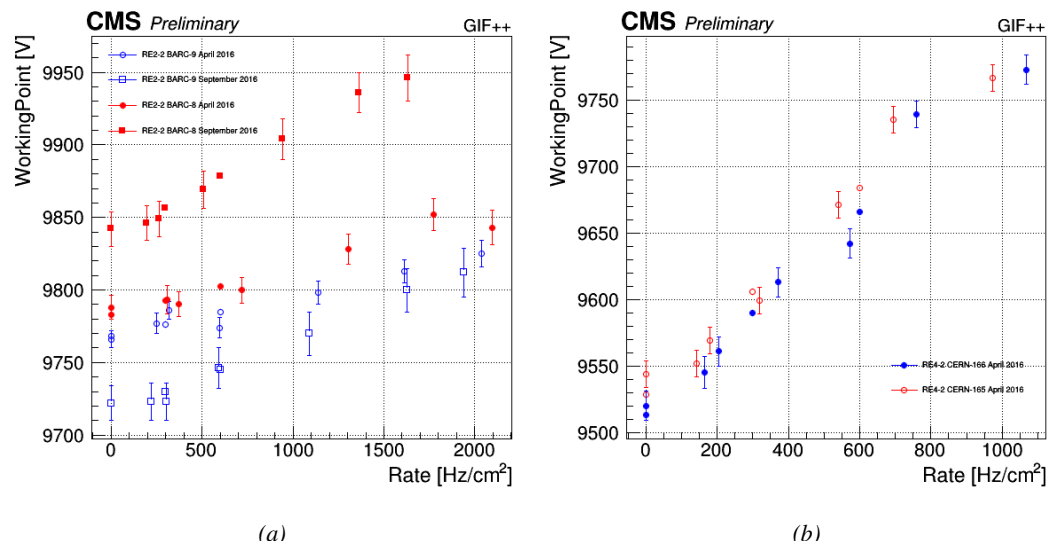


Figure 5.17: Evolution of the working point for RE2 (5.17a) and RE4 (5.17b) with increasing extrapolated  $\gamma$  rate per unit area at working point. Both irradiated (blue) and non irradiated (red) chambers are shown.

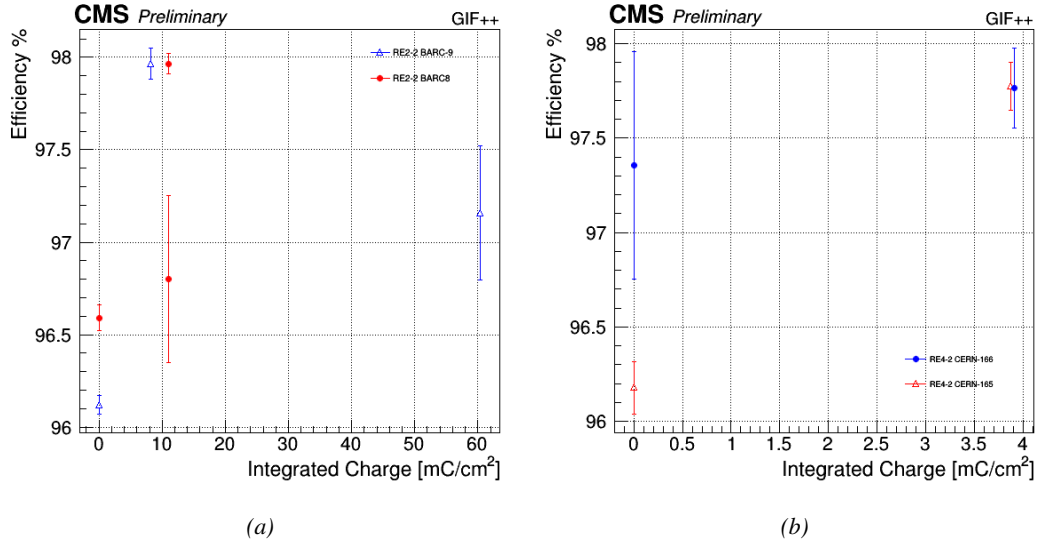


Figure 5.18: Evolution of the maximum efficiency at HL-LHC conditions, i.e. a background hit rate per unit area of  $300 \text{ Hz}/\text{cm}^2$ , with increasing integrated charge for RE2 (5.18a) and RE4 (5.18b) detectors. Both irradiated (blue) and non irradiated (red) chambers are shown. The integrated charge for non irradiated detectors is recorded during test beam periods and stays small with respect to the charge accumulated in irradiated chambers.

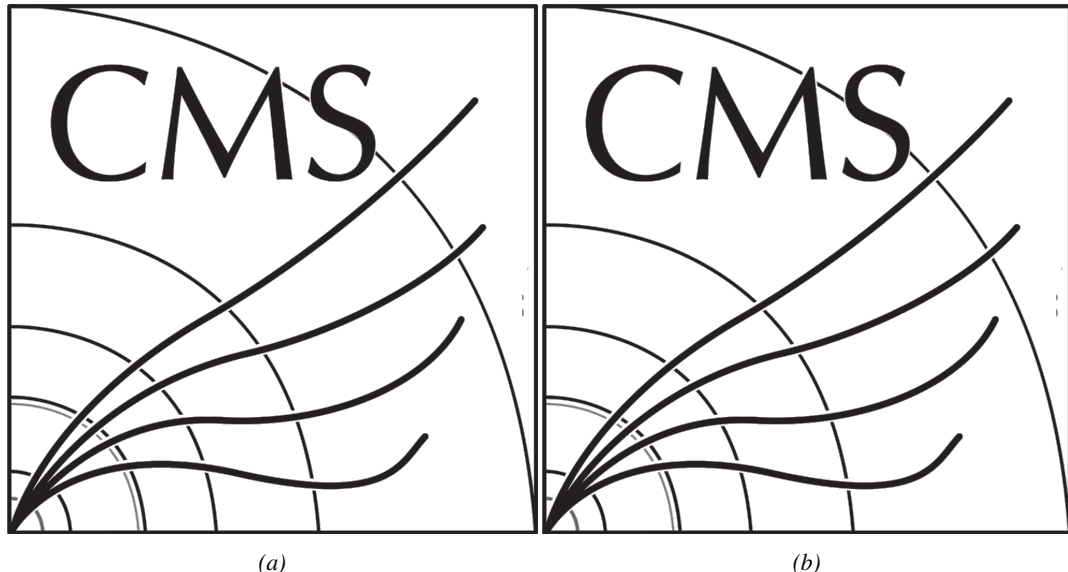


Figure 5.19: Comparison of the efficiency sigmoid before (triangles) and after (circles) irradiation for RE2 (5.19a) and RE4 (5.19b) detectors. Both irradiated (blue) and non irradiated (red) chambers are shown.

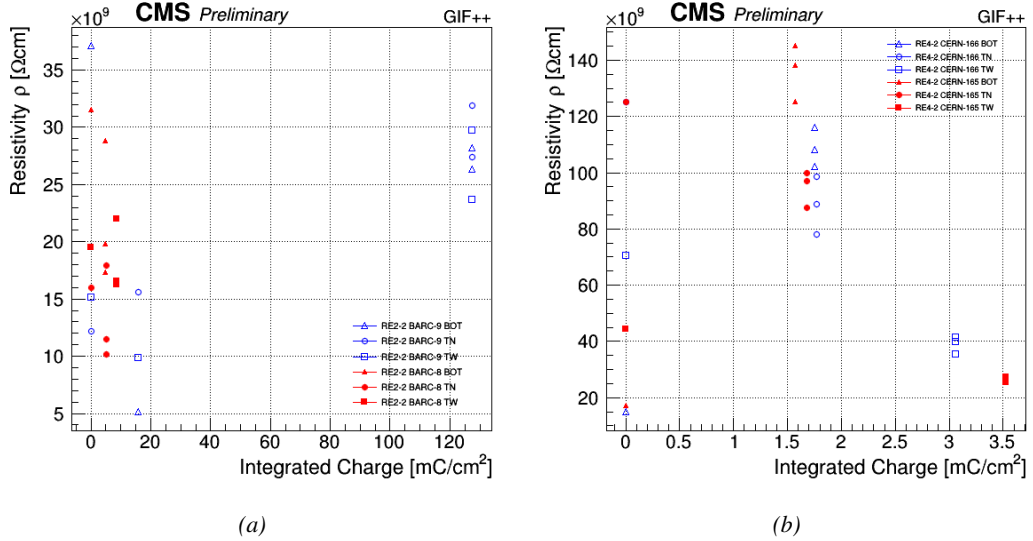


Figure 5.20: Evolution of the Bakelite resistivity for RE2 (5.20a) and RE4 (5.20b) detectors. Both irradiated (blue) and non-irradiated (red) chambers are shown.

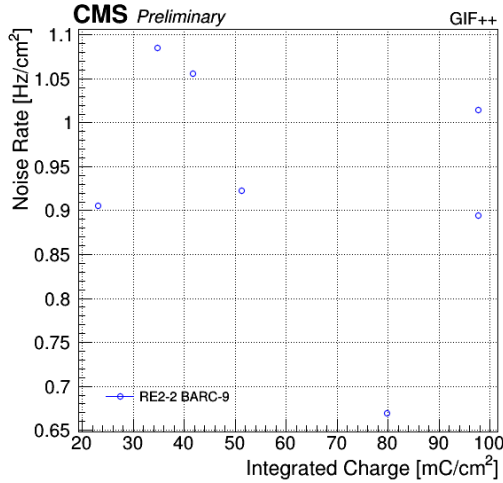


Figure 5.21: Evolution of the noise rate per unit area for the irradiated chamber RE2-2-BARC-9 only.

### 5.3.1 Description of the Data Acquisition

For the longevity studies, four spare chambers of the present system are used. Two spare RPCs of the RE2,3 stations as well as two spare RPCs from the new RE4 stations have been mounted in a Trolley. Six RE4 gaps are also placed in the trolley. The trolley is placed inside the GIFT++ in the upstream region of the bunker, taking the cesium source as a reference. The trolley is oriented for the detection surface of the chambers to be orthogonal to the beam line. The system can be moved along the orthogonal plane in order to have the beam in all  $\eta$ -partitions. For the aging the trolley is

748 moved outside the beam line and is placed in a distance of 5.2 m to the source, which irradiates the  
 749 bunker using an attenuation filter of 2.2 which corresponds to a fluence of  $10^7 \text{ gamma/cm}^2$ .

750 During GIF++ operation, the data collected can be divided into different categories as several  
 751 parameters are monitored in addition to the usual RPC performance data. On one hand, to know  
 752 the performance of a chamber, it is need to measure its efficiency and to know the background  
 753 conditions in which it is operated. To do this, the hit signals from the chamber are recorded and  
 754 stored in a ROOT file via a Data Acquisition (DAQ) software. On the other hand, it is also very  
 755 important to monitor parameters such as environmental pressure and temperature, gas temperature  
 756 and humidity, RPC HV, LV, and currents, or even source and beam status. This is done through the  
 757 GIF++ web Detector Control Software (DCS) that stores this information in a database.

758 Two different types of tests are conducted on RPCs via the DAQ. Indeed, the performance of the  
 759 detectors is measured periodically during dedicated test beam periods using the H4 muon beam. In  
 760 between these test beam periods, when the beam is not available, the chambers are irradiated by the  
 761  $^{137}\text{Cs}$  in order to accumulate deposited charge and the gamma background is measured.

762 RPCs under test are connected through LVDS cables to V1190A Time-to-Digital Converter  
 763 (TDC) modules manufactured by CAEN. These modules, located in the rack area outside of the  
 764 bunker, get the logic signals sent by the chambers and save them into their buffers. Due to the  
 765 limited size of the buffers, the collected data is regularly erased and replaced. A trigger signal is  
 766 needed for the TDC modules to send the useful data to the DAQ computer via a V1718 CAEN USB  
 767 communication module.

768 In the case of performance test, the trigger signal used for data acquisition is generated by the  
 769 coincidence of three scintillators. A first one is placed upstream outside of the bunker, a second one  
 770 is placed downstream outside of the bunker, while a third one is placed in front of the trolley, close by  
 771 the chambers. Every time a trigger is sent to the TDCs, i.e. every time a muon is detected, knowing  
 772 the time delay in between the trigger and the RPC signals, signals located in the right time window  
 773 are extracted from the buffers and saved for later analysis. Signals are taken in a time window of  
 774 400 ns centered on the muon peak (here we could show a time spectrum). On the other hand, in the  
 775 case of background rate measurement, the trigger signal needs to be "random" not to measure muons  
 776 but to look at gamma background. A trigger pulse is continuously generated at a rate of 300 Hz using  
 777 a dual timer. To integrate an as great as possible time, all signals contained within a time window of  
 778 10us prior to the random trigger signal are extracted form the buffers and saved for further analysis  
 779 (here another time spectrum to illustrate could be useful, maybe even place both spectrum together  
 780 as a single Figure).

781 The signals sent to the TDCs correspond to hit collections in the RPCs. When a particle hits  
 782 a RPC, it induce a signal in the pickup strips of the RPC readout. If this signal is higher than the  
 783 detection threshold, a LVDS signal is sent to the TDCs. The data is then organised into 4 branches  
 784 keeping track of the event number, the hit multiplicity for the whole setup, and the time and channel  
 785 profile of the hits in the TDCs.

### 786 5.3.2 RPC current, environmental and operation parameter monitoring

787 In order to take into account the variation of pressure and temperature between different data taking  
 788 periods the applied voltage is corrected following the relationship :

$$789 \text{HV}_{\text{eff}} = \text{HV}_{\text{app}} \times \left( 0.2 + 0.8 \cdot \frac{P_0}{P} \times \frac{T}{T_0} \right) \quad (5.10)$$

789 where  $T_0$  (=293 K) and  $P_0$  (=990 mbar) are the reference values.

790 **5.3.3 Measurement procedure**

791 Insert a short description of the online tools (DAQ, DCS, DQM).

792 Insert a short description of the offline tools : tracking and efficiency algorithm.

793 Identify long term aging effects we are monitoring the rates per strip.

794 **5.3.4 Longevity studies results**



# 6

795

796

## Investigation on high rate RPCs

797 **6.1 Rate limitations and ageing of RPCs**

798 **6.1.1 Low resistivity electrodes**

799 **6.1.2 Low noise front-end electronics**

800 **6.2 Construction of prototypes**

801 **6.3 Results and discussions**



# 7

802

803

## Conclusions and outlooks

804 **7.1 Conclusions**

805 **7.2 Outlooks**



## References

- 807 [1] CERN. Geneva. LHC Experiments Committee. *The CMS muon project : Technical Design*  
808 *Report*. Tech. rep. CERN-LHCC-97-032. CMS Collaboration, 1997.
- 809 [2] CERN. Geneva. LHC Experiments Committee. *Technical Proposal for the Phase-II Upgrade*  
810 *of the CMS Detector*. Tech. rep. CERN-LHCC-2015-010. CMS Collaboration, 2015.
- 811 [3] CERN. Geneva. LHC Experiments Committee. *CMS, the Compact Muon Solenoid : technical*  
812 *proposal*. Tech. rep. CERN-LHCC-94-38. CMS Collaboration, 1994.
- 813 [4] M. Abbrescia et al. “Study of long-term performance of CMS RPC under irradiation at the  
814 CERN GIF”. In: *NIMA* 533 (2004), pp. 102–106.
- 815 [5] H.C. Kim et al. “Quantitative aging study with intense irradiation tests for the CMS forward  
816 RPCs”. In: *NIMA* 602 (2009), pp. 771–774.
- 817 [6] S. Agosteo et al. “A facility for the test of large-area muon chambers at high rates”. In: *NIMA*  
818 452 (2000), pp. 94–104.
- 819 [7] PoS, ed. *CERN GIF ++ : A new irradiation facility to test large-area particle detectors for*  
820 *the high-luminosity LHC program*. Vol. TIPP2014. 2014, pp. 102–109.
- 821 [8] M. Abbrescia et al. “Cosmic ray tests of double-gap resistive plate chambers for the CMS  
822 experiment”. In: *NIMA* 550 (2005), pp. 116–126.
- 823 [9] A. Fagot. *GIF++ DAQ v4.0*. 2017. URL: [https://github.com/afagot/GIF\\_DAQ](https://github.com/afagot/GIF_DAQ).
- 824 [10] CAEN. *Mod. V1190-VX1190 A/B, 128/64 Ch Multihit TDC*. 14th ed. 2016.
- 825 [11] CAEN. *Mod. V1718 VME USB Bridge*. 9th ed. 2009.
- 826 [12] W-Ie-Ne-R. *VME 6021-23 VXI*. 5th ed. 2016.
- 827 [13] Wikipedia. *INI file*. 2017. URL: [https://en.wikipedia.org/wiki/INI\\_file](https://en.wikipedia.org/wiki/INI_file).
- 828 [14] S. Carrillo A. Fagot. *GIF++ Offline Analysis v6*. 2017. URL: [https://github.com/afagot/GIF\\_OfflineAnalysis](https://github.com/afagot/GIF_OfflineAnalysis).



# A

830

831

## A data acquisition software for CAEN VME TDCs

832

833 Certifying detectors in the perspective of HL-LHC required to develop tools for the GIF++ experiment.  
834 Among them was the C++ Data Acquisition (DAQ) software that allows to make the com-  
835 munications in between a computer and TDC modules in order to retrieve the RPC data [9]. In this  
836 appendix, details about this software, as of how the software was written, how it functions and how  
837 it can be exported to another similar setup, will be given.

### 838 A.1 GIF++ DAQ file tree

839 GIF++ DAQ source code is fully available on github at [https://github.com/afagot/GIF\\_](https://github.com/afagot/GIF_DAQ)  
840 DAQ. The software requires 3 non-optional dependencies:

- 841 • CAEN USB Driver, to mount the VME hardware,  
842 • CAEN VME Library, to communicate with the VME hardware, and  
843 • ROOT, to organize the collected data into a TTree.

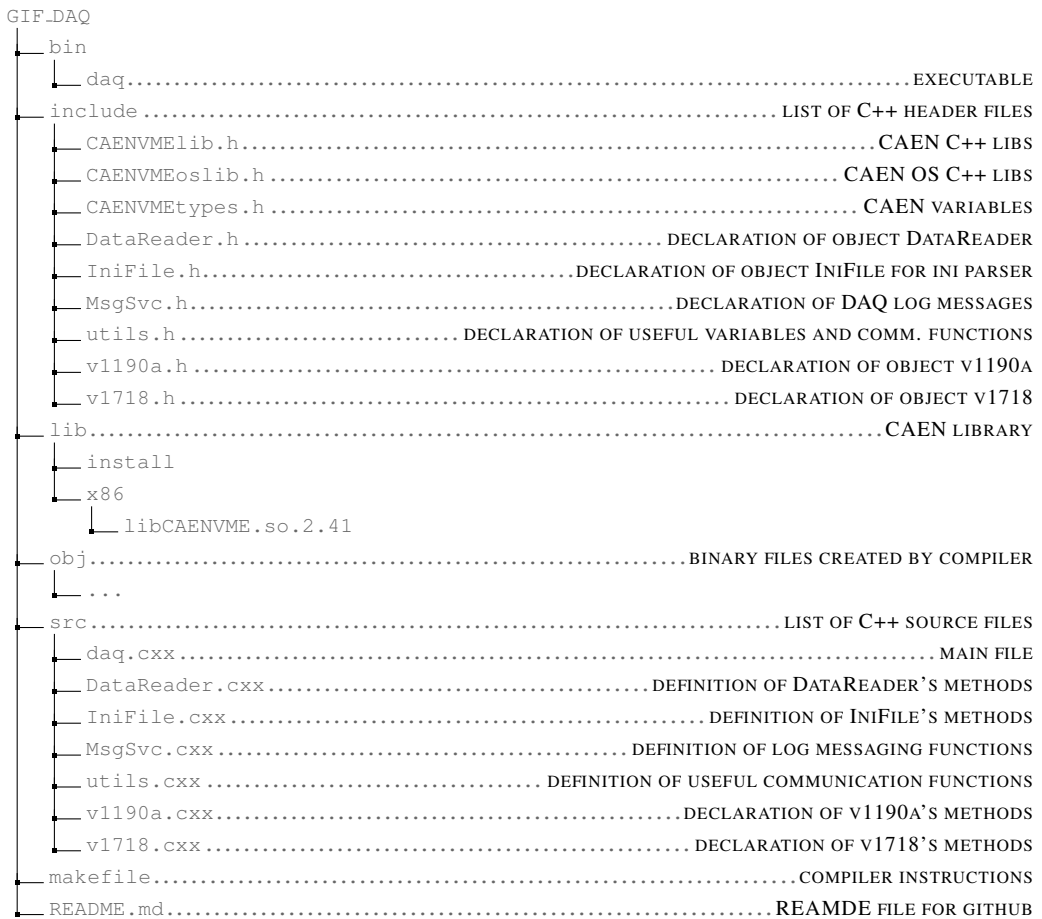
844 The CAEN VME library will not be packaged by distributions and will need to be installed man-  
845 ually. To compile the GIF++ DAQ project via a terminal, from the DAQ folder use the command:

846

```
847     make
```

848 The source code tree is provided below along with comments to give an overview of the files' con-  
849 tent. The different objects created for this project (`v1718`, `v1190a`, `IniFile` & `DataReader`) will be  
850 described in details in the following sections.

851



## 852    A.2    Usage of the DAQ

853    GIF++ DAQ, as used in GIF++, is not a standalone software. Indeed, the system being more complexe,  
 854    the DAQ only is a sub-layer of the software architecture developped to control and monitor  
 855    the RPCs that are placed into the bunker for performance study in an irradiated environment. The top  
 856    layer of GIF++ is a Web Detector Control System (webDCS) application. The DAQ is only called  
 857    by the webDCS when data needs to be acquired. The webDCS operates the DAQ through command  
 858    line. To start the DAQ, the webDCS calls:

859

860       bin/daq /path/to/the/log/file/in/the/output/data/folder

861    where /path/to/the/log/file/in/the/output/data/folder is the only argument required. This  
 862    log file is important for the webDCS as this file contains all the content of the communication of the  
 863    webDCS and the different systems monitored by the webDCS. Its content is constantly displayed  
 864    during data taking for the users to be able to follow the operations. The communication messages  
 865    are normally sent to the webDCS log file via the functions declared in file MsgSvc.h, typically  
 866    MSG\_INFO(string message).

867

### 868 A.3 Description of the readout setup

869 The CMS RPC setup at GIF++ counts 5 V1190A Time-to-Digital Converter (TDC) manufactured  
 870 by CAEN [10]. V1190A are VME units accepting 128 independent Multi-Hit/Multi-Event TDC  
 871 channels whose signals are treated by 4 100 ps high performance TDC chips developed by CERN  
 872 / ECP-MIC Division. The communication between the computer and the TDCs to transfer data is  
 873 done via a V1718 VME master module also manufactured by CAEN and operated from a USB  
 874 port [11]. These VME modules are all hosted into a 6U VME 6021 powered crate manufactured by  
 875 W-Ie-Ne-R than can accommodate up to 21 VME bus cards [12]. These 3 components of the DAQ  
 876 setup are shown in Figure A.1.

877

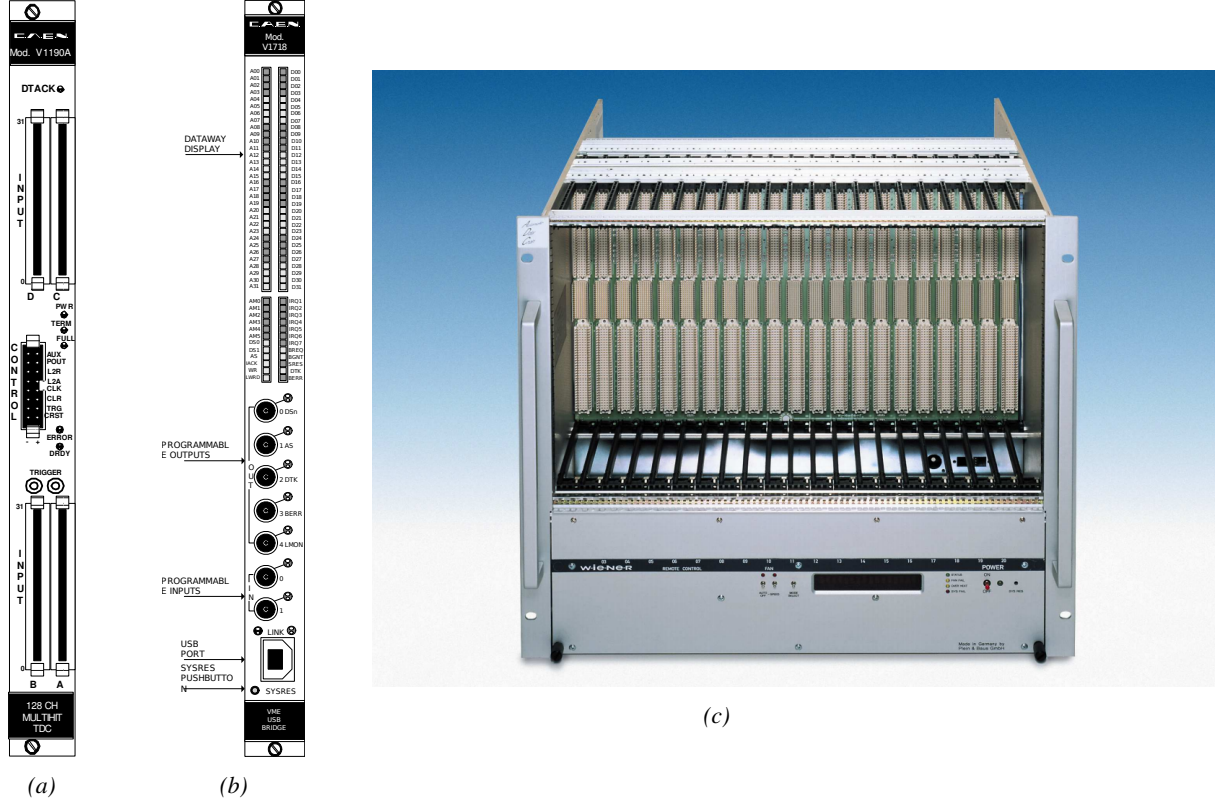


Figure A.1: (A.1a) View of the front panel of a V1190A TDC module [10]. (A.1b) View of the front panel of a V1718 Bridge module [11]. (A.1c) View of the front panel of a 6U 6021 VME crate [12].

878

### A.4 Data read-out

879 To efficiently perform a data readout algorithm, C++ objects to handle the VME modules (TDCs  
 880 and VME bridge) have been created along with objects to store data and read the configuration file

881 that comes as an input of the DAQ software.

882

### 883 A.4.1 V1190A TDCs

884 The DAQ used at GIF takes profit of the *Trigger Matching Mode* offered by V1190A modules.  
 885 This setting is enabled through the method `v1190a::SetTrigMatching (int ntdcs)` where `ntdcs`  
 886 is the total number of TDCs in the setup this setting needs to be enabled for (Source Code A.1). A  
 887 trigger matching is performed in between a trigger time tag, a trigger signal sent into the TRIGGER  
 888 input of the TDC visible on Figure A.1a, and the channel time measurements, signals recorded from  
 889 the detectors under test in our case. Control over this data acquisition mode, explained through  
 890 Figure A.2, is offered via 4 programmable parameters:

- 891 • **match window:** the matching between a trigger and a hit is done within a programmable time  
 892 window. This is set via the method

```
893     void v1190a::SetTrigWindowWidth(UINT windowWidth, int ntdcs)
```

- 894 • **window offset:** temporal distance between the trigger tag and the start of the trigger matching  
 895 window. This is set via the method

```
896     void v1190a::SetTrigWindowWidth(UINT windowWidth, int ntdcs)
```

- 897 • **extra search margin:** an extended time window is used to ensure that all matching hits are  
 898 found. This is set via the method

```
899     void v1190a::SetTrigSearchMargin(UINT searchMargin, int ntdcs)
```

- 900 • **reject margin:** older hits are automatically rejected to prevent buffer overflows and to speed  
 901 up the search time. This is set via the method

```
902     void v1190a::SetTrigRejectionMargin(UINT rejectMargin, int ntdcs)
```

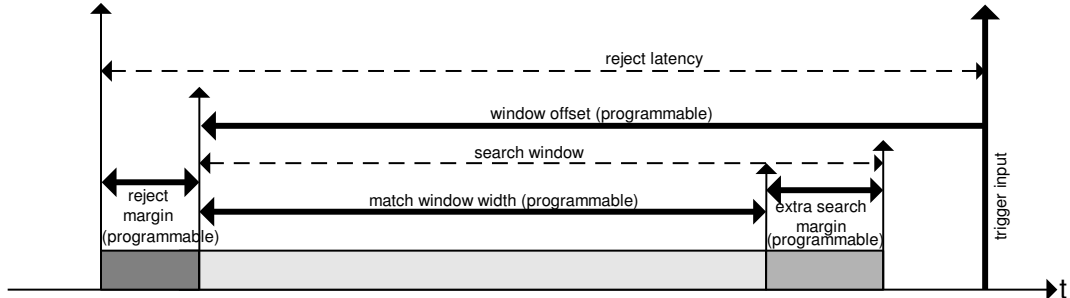


Figure A.2: Module V1190A Trigger Matching Mode timing diagram [10].

903 Each of these 4 parameters are given in number of clocks, 1 clock being 25 ns long. It is easy to  
 904 understand at this level that there are 3 possible functioning settings:

- 905 • **1:** the match window is entirely contained after the trigger signal,

- 906 • **2:** the match window overlaps the trigger signal, or

- 907 • **3:** the match window is entirely contained before the trigger signal as displayed on Figure A.2.

908 In both the first and second cases, the sum of the window width and of the offset can be set to  
909 a maximum of 40 clocks, which corresponds to 1  $\mu$ s. Evidently, the offset can be negative, allowing  
910 for a longer match window, with the constraint of having the window ending at most 1  $\mu$ s after the  
911 trigger signal. In the third case, the maximum negative offset allowed is of 2048 clocks (12 bit) cor-  
912 responding to 51.2  $\mu$ s, the match window being strictly smaller than the offset. In the case of GIF++,  
913 the choice has been made to use this last setting by delaying the trigger signal. During the studies  
914 performed in GIF++, both the efficiency of the RPCs, probed using a muon beam, and the noise or  
915 gamma background rate are monitored. The extra search and reject margins are left unused.  
916 To probe the efficiency of RPC detectors, the trigger time tag is provided by the coïncidence of  
917 scintillators when a bunch of muons passes through GIF++ area is used to trigger the data acquisi-  
918 tion. For this measurement, it is useful to reduce the match window width only to contain the muon  
919 information. Indeed, the delay in between a trigger signal and the detection of the corresponding  
920 muon in the RPC being very contant (typically a few tens of ns due to jitter and cable length), the  
921 muon signals are very localised in time. Thus, due to a delay of approximalety 325 ns in between  
922 the muons and the trigger, the settings where chosen to have a window width of 24 clocks (600 ns)  
923 centered on the muon peak thanks to a negative offset of 29 clocks (725 ns).  
924 On the otherhand, monitoring the rates don't require for the DAQ to look at a specific time window.  
925 It is important to integrate enough time to have a robust measurement of the rate as the number of  
926 hits per time unit. The triggerring signal is provided by a pulse generator at a frequency of 300 Hz  
927 to ensure that the data taking occurs in a random way, with respect to beam physics, to probe only  
928 the irradiation spectrum on the detectors. The match window is set to 400 clocks (10  $\mu$ s) and the  
929 negative offset to 401 clocks as it needs to exceed the value of the match window.

```

930
class v1190a
{
private :
    long             Handle;
    vector<Data32>   Address;
    CVDataWidth      DataWidth;
    CVAddressModifier AddressModifier;

public:
    v1190a(long handle, IniFile *inifile, int ntdcs);
    ~v1190a();
    Data16 write_op_reg(Data32 address, int code, string error);
    Data16 read_op_reg(Data32 address, string error);
    void Reset(int ntdcs);
    void Clear(int ntdcs);
    void TestWR(Data16 value,int ntdcs);
    void CheckTDCStatus(int ntdcs);
    void CheckCommunication(int ntdcs);
    void SetTDCTestMode(Data16 mode,int ntdcs);
    void SetTrigMatching(int ntdcs);
    void SetTrigTimeSubtraction(Data16 mode,int ntdcs);
    void SetTrigWindowWidth(Uint windowHeight,int ntdcs);
    void SetTrigWindowOffset(Uint windowOffset,int ntdcs);
    void SetTrigSearchMargin(Uint searchMargin,int ntdcs);
    void SetTrigRejectionMargin(Uint rejectMargin,int ntdcs);
    void GetTrigConfiguration(int ntdcs);
    void SetTrigConfiguration(IniFile *inifile,int ntdcs);
    void SetTDCDetectionMode(Data16 mode,int ntdcs);
    void SetTDCResolution(Data16 lsb,int ntdcs);
    void SetTDCDeadTime(Data16 time,int ntdcs);
    void SetTDCHeadTrailer(Data16 mode,int ntdcs);
    void SetTDCEventSize(Data16 size,int ntdcs);
    void SwitchChannels(IniFile *inifile,int ntdcs);
    void SetIRQ(Data32 level, Data32 count,int ntdcs);
    void SetBlockTransferMode(Data16 mode,int ntdcs);
    void Set(IniFile *inifile,int ntdcs);
    void CheckStatus(CVErrorCodes status) const;
    int ReadBlockD32(Uint tdc, const Data16 address,
                     Data32 *data, const Uint words, bool ignore_berr);
    Uint Read(RAWData *DataList,int ntdcs);
};

931

```

932       *Source Code A.1: Description of C++ object v1190a.*

933       The v1190a object, defined in the DAQ software as in Source Code A.1, offers the possibility to  
 934       concatenate all TDCs in the readout setup into a single object containing a list of hardware addresses  
 935       (addresses to access the TDCs' buffer through the VME crate) and each constructor and method acts  
 936       on the list of TDCs.  
 937

#### 938      **A.4.2 DataReader**

939      Enabled thanks to v1190a::SetBlockTransferMode(Data16 mode, int ntdcs), the data transfer  
 940      is done via Block Transfer (BLT). Using BLT allows to tranfer a fixed number of events called a  
 941      *block*. This is used together with an Almost Full Level (AFL) of the TDCs' output buffers, defined

942 through `v1190a::SetIRQ(Data32 level, Data32 count, int ntdcs)`. This AFL gives the maxi-  
 943 mum amount of 32735 words (16 bits, corresponding to the depth of a TDC output buffer) that can  
 944 written in a buffer before an Interrupt Request (IRQ) is generated and seen by the VME Bridge,  
 945 stopping the data acquisition to transfer the content of each TDC buffers before resuming. For each  
 946 trigger, 6 words or more are written into the TDC buffer:

- 947     • a **global header** providing information of the event number since the beginning of the data  
       acquisition,
- 949     • a **TDC header**,
- 950     • the **TDC data** (*if any*), 1 for each hit recorded during the event, providing the channel and the  
       time stamp associated to the hit,
- 952     • a **TDC error** providing error flags,
- 953     • a **TDC trailer**,
- 954     • a **global trigger time tag** that provides the absolute trigger time relatively to the last reset,  
       and
- 956     • a **global trailer** providing the total word count in the event.

957     As previously described in Section 4.4.3, CMS RPC FEEs provide us with 100 ns long LVDS  
 958 output signals that are injected into the TDCs' input. Any avalanche signal that gives a signal above  
 959 the FEEs threshold is thus recorded by the TDCs as a hit within the match window. Each hit is  
 960 assigned to a specific TDC channel with a time stamp, with a precision of 100 ps. The reference  
 961 time,  $t_0 = 0$ , is provided by the beginning of the match window. Thus for each trigger, coming from  
 962 a scintillator coïncidence or the pulse generator, a list of hits is stored into the TDCs' buffers and  
 963 will then be transferred into a ROOT Tree.

964  
 965     When the BLT is used, it is easy to understand that the maximum number of words that have  
 966 been set as ALF will not be a finite number of events or, at least, the number of events that would  
 967 be recorded into the TDC buffers will not be a multiple of the block size. In the last BLT cycle to  
 968 tranfer data, the number of events to transfer will most probably be lower than the block size. In that  
 969 case, the TDC can add fillers at the end of the block but this option requires to send more data to the  
 970 computer and is thus a little slower. Another solution is to finish the transfer after the last event by  
 971 sending a bus error that states that the BLT reached the last event in the pile. This method has been  
 972 chosen in GIF++.

973  
 974     Due to irradiation, an event in GIF++ can count up to 300 words per TDC. A limit of 4096 words  
 975 (12 bits) has been set to generate IRQ which represent from 14 to almost 700 events depending on  
 976 the average of hits collected per event. Then the block size has been set to 100 events with enabled  
 977 bus errors. When an AFL is reached for one of the TDCs, the VME bridge stops the acquisition by  
 978 sending a BUSY signal.

979

980     The data is then transferred one TDC at a time into a structure called `RAWData` (Source Code A.2).

```
981
982     struct RAWData{
983         vector<int>           *EventList;
984         vector<int>           *NHitsList;
985         vector<int>           *QFlagList;
986         vector<vector<int>>   *Channellist;
987         vector<vector<float>>  *TimeStampList;
988     };
```

983                 *Source Code A.2: Description of data holding C++ structure `RAWData`.*

984     In order to organize the data transfer and the data storage, an object called `DataReader` was  
985     created (Source Code A.3). On one hand, it has `v1718` and `v1190a` objects as private members for  
986     communication purposes, such as VME modules settings via the configuration file `*iniFile` or data  
987     read-out through `v1190a::Read()` and on the other hand, it contains the structure `RAWData` that allows  
988     to organise the data in vectors reproducing the tree structure of a ROOT file.

```
989
990     class DataReader
991     {
992         private:
993             bool      StopFlag;
994             IniFile *iniFile;
995             Data32  MaxTriggers;
996             v1718   *VME;
997             int       nTDCs;
998             v1190a  *TDCs;
999             RAWData TDCData;
```

```
1000
1001         public:
1002             DataReader();
1003             virtual ~DataReader();
1004             void      SetIniFile(string inifilename);
1005             void      SetMaxTriggers();
1006             Data32  GetMaxTriggers();
1007             void      SetVME();
1008             void      SetTDC();
1009             int       GetQFlag(Uint it);
1010             void      Init(string inifilename);
1011             void      FlushBuffer();
1012             void      Update();
1013             string  GetFileName();
1014             void      WriteRunRegistry(string filename);
1015             void      Run();
```

1016 };

991                 *Source Code A.3: Description of C++ object `DataReader`.*

992     Each event is transferred from `TDCData` and saved into branches of a ROOT `TTree` as 3 integers  
993     that represent the event ID (`EventCount`), the number of hits read from the TDCs (`nHits`), and the  
994     quality flag that provides information for any problem in the data transfer (`qflag`), and 2 lists of  
995     `nHits` elements containing the fired TDC channels (`TDCCh`) and their respective time stamps (`TDCTS`),  
996     as presented in Source Code A.4. The ROOT file file is named using information contained into  
997     the configuration file, presented in section A.5.2. The needed information is extracted using method  
998     `DataReader::GetFileName()` and allow to build the output filename format `ScanXXXXXX_HVX_DAQ.root`

999 where ScanXXXXXX is a 6 digit number representing the scan number into GIF++ database and HVX  
 1000 the HV step within the scan that can be more than a single digit. An example of ROOT data file is  
 1001 provided with Figure A.3.

```
1002
RAWData TDCData;
TFile *outputFile = new TFile(outputFileName.c_str(),"recreate");
TTree *RAWDataTree = new TTree("RAWData","RAWData");

int EventCount = -9;
int nHits = -8;
int qflag = -7;
vector<int> TDCCh;
vector<float> TDCTS;

RAWDataTree->Branch("EventNumber",&EventCount, "EventNumber/I");
RAWDataTree->Branch("number_of_hits",&nHits,"number_of_hits/I");
RAWDataTree->Branch("Quality_flag",&qflag,"Quality_flag/I");
RAWDataTree->Branch("TDC_channel",&TDCCh);
RAWDataTree->Branch("TDC_TimeStamp",&TDCTS);

1003
//...
//Here read the TDC data using v1190a::Read() and place it into
//TDCData for as long as you didn't collect the requested amount
//of data.
//...

for(Uint i=0; i<TDCData.EventList->size(); i++){
    EventCount = TDCData.EventList->at(i);
    nHits = TDCData.NHitsList->at(i);
    qflag = TDCData.QFlagList->at(i);
    TDCCh = TDCData.ChannelList->at(i);
    TDCTS = TDCData.TimeStampList->at(i);
    RAWDataTree->Fill();
}
```

1004 *Source Code A.4: Highlight of the data transfer and organisation within DataReader::Run() after the data has been collected into TDCData.*

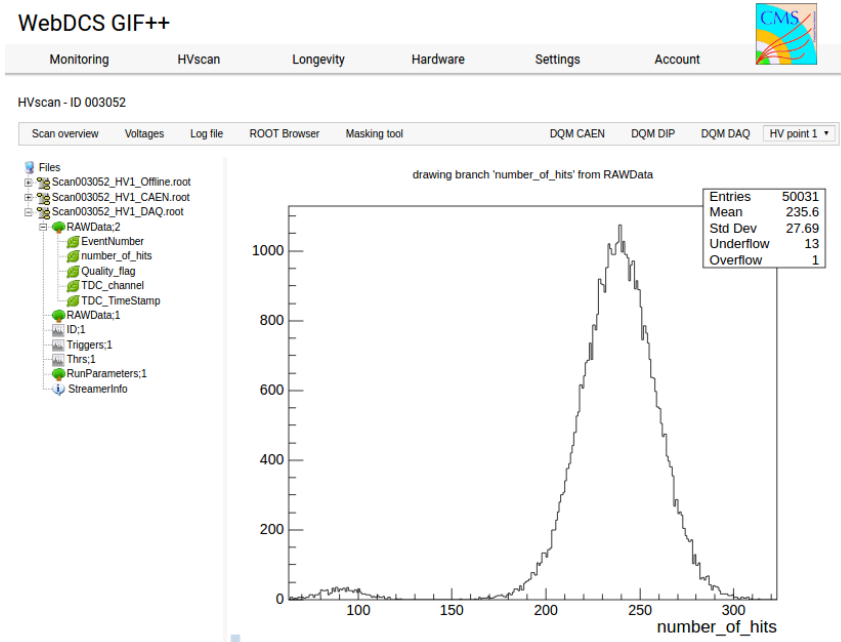


*Figure A.3: Structure of the ROOT output file generated by the DAQ. The 5 branches (EventNumber, number\_of\_hits, Quality\_flag, TDC\_channel and TDC\_TimeStamp) are visible on the left panel of the ROOT browser. On the right panel is visible the histogram corresponding to the variable nHits. In this specific example, there were approximately 50k events recorded to measure the gamma irradiation rate on the detectors. Each event is stored as a single entry in the TTree.*

## 1005 A.5 Communications

1006 To ensure data readout and dialog in between the machine and the TDCs or in between the webDCS  
 1007 and the DAQ, different communication solutions were used. First of all, it is important to have a  
 1008 module to allow the communication in between the TDCs and the computer from which the DAQ  
 1009 operates. When this communication is effective, shifters using the webDCS to control data taking  
 1010 can thus send instructions to the DAQ.

1011

### 1012 A.5.1 V1718 USB Bridge

1013 In the previous section, the data transfer has been discussed. The importance of the `v1718` object  
 1014 (Source Code A.5), used as private member of `DataReader`, was not explicated. VME master  
 1015 modules are used for communication purposes as they host the USB port that connects the pow-  
 1016 ered crate buffer to the computer where the DAQ is installed. From the source code point of view,  
 1017 this object is used to control the communication status, by reading the returned error codes with  
 1018 `v1718::CheckStatus()`, or to check for IRQs coming from the TDCs through `v1718::CheckIRQ()`.  
 1019 Finally, to ensure that triggers are blocked at the hardware level, a NIM pulse is sent out of one of the  
 1020 5 programmable outputs (`v1718::SendBUSY()`) to the VETO of the coincidence module where the  
 1021 trigger signals originate from. As long as this signal is ON, no trigger can reach the TDCs anymore.

```

1022
class v1718{
    private:
        int             Handle;
        Data32          Data;           // Data
        CVIRQLevels     Level;         // Interrupt level
        CVAddressModifier AM;          // Addressing Mode
        CVDataWidth     dataSize;      // Data Format
        Data32          BaseAddress;   // Base Address

    public:
        v1718(IniFile *inifile);
        ~v1718();
        long            GetHandle(void) const;
        int             SetData(Data16 data);
        Data16          GetData(void);
        int             SetLevel(CVIRQLevels level);
        CVIRQLevels     GetLevel(void);
        int             SetAM(CVAddressModifier am);
        CVAddressModifier GetAM(void);
        int             SetDatasize(CVDataWidth datasize);
        CVDataWidth     GetDataSize(void);
        int             SetBaseAddress(Data16 baseaddress);
        Data16          GetBaseAddress(void);
        void            CheckStatus(CVErrorCodes status) const;
        bool            CheckIRQ();
        void            SetPulsers();
        void            SendBUSY(BusyLevel level);
};

1023
1024

```

*Source Code A.5: Description of C++ object v1718.*

## 1025 A.5.2 Configuration file

1026 The DAQ software takes as input a configuration file written using INI standard [13]. This file is  
 1027 partly filled with the information provided by the shifters when starting data acquisition using the  
 1028 webDCS, as shown by Figure A.4. This information is written in section [**General**] and will later  
 1029 be stored in the ROOT file that contains the DAQ data as can be seen from Figure A.3. Indeed,  
 1030 another TTree called `RunParameters` as well as the 2 histograms `ID`, containing the scan number,  
 1031 start and stop time stamps, and `Triggers`, containing the number of triggers requested by the shifter,  
 1032 are available in the data files. Moreover, `ScanID` and `HV` are then used to construct the file name  
 1033 thanks to the method `DataReader::GetFileName()`.

WebDCS GIF++

---

Monitoring    HVscan    Longevity    Hardware    Settings    Account



DAQ High Voltage Scan

|                       |                                   |                                   |                                 |   |     |
|-----------------------|-----------------------------------|-----------------------------------|---------------------------------|---|-----|
| Type scan:            | Rate Scan                         | Comments:                         |                                 |   |     |
| Source configuration: | Source OFF                        | U                                 | 333                             | D | 333 |
| Beam configuration:   | Beam OFF                          |                                   |                                 |   |     |
| Waiting time:         | 1                                 | (min)                             |                                 |   |     |
| Trigger mode:         | <input type="checkbox"/> External | <input type="checkbox"/> Internal | <input type="checkbox"/> Random |   |     |
| Minimal measure time: | 10                                | (min)                             |                                 |   |     |

| Chamber              | RE2-2-NPD-BARC-8 | RE2-2-CERN-105 | RE2-2-NPD-BARC-9 | RE4-2-CERN-105 | RE4-2-KODEL-1-4 | Max triggers |
|----------------------|------------------|----------------|------------------|----------------|-----------------|--------------|
| HV <sub>eff</sub> 1  | 8600             | 8500           | 8600             | 8500           | 6500            |              |
| HV <sub>eff</sub> 2  | 8700             | 8600           | 8700             | 8600           | 6600            |              |
| HV <sub>eff</sub> 3  | 8800             | 8700           | 8800             | 8700           | 6700            |              |
| HV <sub>eff</sub> 4  | 8900             | 8800           | 8900             | 8800           | 6800            |              |
| HV <sub>eff</sub> 5  | 9000             | 8900           | 9000             | 8900           | 6900            |              |
| HV <sub>eff</sub> 6  | 9100             | 9000           | 9100             | 9000           | 7000            |              |
| HV <sub>eff</sub> 7  | 9200             | 9100           | 9200             | 9100           | 7100            |              |
| HV <sub>eff</sub> 8  | 9300             | 9200           | 9300             | 9200           | 7200            |              |
| HV <sub>eff</sub> 9  | 9400             | 9300           | 9400             | 9300           | 7300            |              |
| HV <sub>eff</sub> 10 | 9500             | 9400           | 9500             | 9400           | 7400            |              |

**Start HV scan**

*Figure A.4: WebDCS DAQ scan page. On this page, shifters need to choose the type of scan (Rate, Efficiency or Noise Reference scan), the gamma source configuration at the moment of data taking, the beam configuration, and the trigger mode. These information will be stored in the DAQ ROOT output. Are also given the minimal measurement time and waiting time after ramping up of the detectors is over before starting the data acquisition. Then, the list of HV points to scan and the number of triggers for each run of the scan are given in the table underneath.*

1034      The rest of the information is written beforehand in the configuration file template, as explicated  
 1035      in Source Code A.6, and contains the hardware addresses to the different VME modules in the  
 1036      setup as well as settings for the TDCs. As the TDC settings available in the configuration file are not  
 1037      supposed to be modified, an improvement would be to remove them from the configuration file and  
 1038      to hardcode them inside of the DAQ code itself or to place them into a different INI file that would  
 1039      host only the TDC settings to lower the probability for a bad manipulation of the configuration file  
 1040      that can be modified from one of webDCS' menus.

```
1041
[General]
TdcS=4
ScanID=$scanid
HV=$HV
RunType=$runtype
MaxTriggers=$maxtriggers
Beam=$beam
[VMEInterface]
Type=V1718
BaseAddress=0xFF0000
Name=VmeInterface
[TDC0]
Type=V1190A
BaseAddress=0x00000000
Name=Tdc0
StatusA00-15=1
StatusA16-31=1
StatusB00-15=1
StatusB16-31=1
StatusC00-15=1
StatusC16-31=1
StatusD00-15=1
StatusD16-31=1
[TDC1]
Type=V1190A
BaseAddress=0x11110000
Name=Tdc1
StatusA00-15=1
StatusA16-31=1
StatusB00-15=1
StatusB16-31=1
StatusC00-15=1
StatusC16-31=1
StatusD00-15=1
StatusD16-31=1
1042
[TDC2]
Type=V1190A
BaseAddress=0x22220000
Name=Tdc2
StatusA00-15=1
StatusA16-31=1
StatusB00-15=1
StatusB16-31=1
StatusC00-15=1
StatusC16-31=1
StatusD00-15=1
StatusD16-31=1
[TDC3]
Type=V1190A
BaseAddress=0x44440000
Name=Tdc3
StatusA00-15=1
StatusA16-31=1
StatusB00-15=1
StatusB16-31=1
StatusC00-15=1
StatusC16-31=1
StatusD00-15=1
StatusD16-31=1
[TDCSettings]
TriggerExtraSearchMargin=0
TriggerRejectMargin=0
TriggerTimeSubtraction=0b1
TdcDetectionMode=0b01
TdcResolution=0b10
TdcDeadTime=0b00
TdcHeadTrailer=0b1
TdcEventSize=0b1001
TdcTestMode=0b0
BLTMode=1
```

*Source Code A.6: INI configuration file template for 4 TDCs. In section [General], the number of TDCs is explicitated and information about the ongoing run is given. Then, there are sections for each and every VME modules. There buffer addresses are given and for the TDCs, the list of channels to enable is given. Finally, in section [TDCSettings], a part of the TDC settings are given.*

1044     In order to retrieve the information of the configuration file, the object `IniFile` has been developed  
 1045     to provide an INI parser, presented in Source Code A.7. It contains private methods returning a  
 1046     boolean to check the type of line written in the file, whether a comment, a group header or a key line  
 1047     (`IniFile::CheckIfComment()`, `IniFile::CheckIfGroup()` and `IniFile::CheckIfToken()`). The  
 1048     key may sometimes be referred to as *token* in the source code. Moreover, the private element  
 1049     `FileData` is a map of `const string` to `string` that allows to store the data contained inside the  
 1050     configuration file via the public method `IniFile::GetFileData()` following the formatting (see  
 1051     method `IniFile::Read()`):

```
1052
  1053     string group, token, value;
  // Get the field values for the 3 strings.
  // Then concatenate group and token together as a single string
  // with a dot separation.
  token = group + "." + token;
  FileData[token] = value;
```

1054     More methods have been written to translate the different keys into the right variable format  
 1055     when used by the DAQ. For example, to get a `float` value out of the configuration file data, knowing  
 1056     the group and the key needed, the method `IniFile::floatType()` can be used. It takes 3 arguments  
 1057     being the group name and key name (both `string`), and a default `float` value used as exception in  
 1058     the case the expected combination of group and key cannot be found in the configuration file. This  
 1059     default value is then used and the DAQ continues on working after sending an alert in the log file for  
 1060     further debugging.

```

1061 typedef map< const string, string > IniFileData;
1062
class IniFile{
    private:
        bool          CheckIfComment (string line);
        bool          CheckIfGroup(string line, string& group);
        bool          CheckIfToken(string line, string& key, string& value);
        string         FileName;
        IniFileData   FileData;
        int           Error;

    public:
        IniFile();
        IniFile(string filename);
        virtual      ~IniFile();

        // Basic file operations
        void          SetFileName(string filename);
        int           Read();
        int           Write();
        IniFileData GetFileData();

        // Data readout methods
        Data32         addressType (string groupname, string keyname, Data32
→     defaultvalue);
        long          intType     (string groupname, string keyname, long
→     defaultvalue);
        long long    longType    (string groupname, string keyname, long long
→     defaultvalue );
        string         stringType  (string groupname, string keyname, string
→     defaultvalue );
        float         floatType   (string groupname, string keyname, float
→     defaultvalue );

        // Error methods
        string         GetErrorMsg();
    };

```

1063       *Source Code A.7: Description of C++ object `IniFile` used as a parser for INI file format.*

### 1064       A.5.3 WebDCS/DAQ intercommunication

1065       When shifters send instructions to the DAQ via the configuration file, it is the webDCS itself that  
 1066       gives the start command to the DAQ and then the 2 softwares use inter-process communication  
 1067       through file to synchronise themselves. This communication file is represented by the variable **const**  
 1068       **string** \_\_runstatuspath.

1069       On one side, the webDCS sends commands or status that are readout by the DAQ:

- 1070       • INIT, status sent when launching a scan and read via function `CtrlRunStatus(...)`,
- 1071       • START, command to start data taking and read via function `CheckSTART()`,
- 1072       • STOP, command to stop data taking at the end of the scan and read via function `CheckSTOP()`,  
 1073        and
- 1074       • KILL, command to kill data taking sent by user and read via function `CheckKILL()`

1075 and on the other, the DAQ sends status that are controled by the webDCS:

- 1076     ● `DAQ_RDY`, sent with `SendDAQReady()` to signify that the DAQ is ready to receive commands  
1077       from the webDCS,
- 1078     ● `RUNNING`, sent with `SendDAQRunning()` to signify that the DAQ is taking data,
- 1079     ● `DAQ_ERR`, sent with `SendDAQError()` to signify that the DAQ didn't receive the expected com-  
1080       mand from the webDCS or that the launch command didn't have the right number of argu-  
1081       ments,
- 1082     ● `RD_ERR`, sent when the DAQ wasn't able to read the communication file, and
- 1083     ● `WR_ERR`, sent when the DAQ wasn't able to write into the communication file.

#### 1084 **A.5.4 Example of inter-process communication cycle**

1085 Under normal conditions, the webDCS and the DAQ processes exchange commands and status via  
1086 the file hosted at the address `__runstatuspath`, as explained in subsection A.5.3. An example of  
1087 cycle is given in Table A.1. In this example, the steps 3 to 5 are repeated as long as the webDCS tells  
1088 the DAQ to take data. A data taking cycle is the equivalent as what is called a *Scan* in GIFT++ jargon,  
1089 referring to a set a runs with several HV steps. Each repetition of steps 3 to 5 is then equivalent to a  
1090 single *Run*.

1091

1092 At any moment during the data taking, for any reason, the shifter can decide that the data taking  
1093 needs to be stopped before it reached the end of the scheduled cycle. Thus at any moment on the  
1094 cycle, the content of the inter-process communication file will be changed to `KILL` and the DAQ will  
1095 shut down right away. The DAQ checks for `KILL` signals every 5s after the TDCs configuration is  
1096 over. So far, the function `CheckKILL()` has been used only inside of the data taking loop of method  
1097 `DataReader::Run()` and thus, if the shifter decides to KILL the data taking during the TDC con-  
1098 figuration phase or the HV ramping in between 2 HV steps, the DAQ will not be stopped smoothly  
1099 and a *force kill* command will be sent to stop the DAQ process that is still awake on the computer.  
1100 Improvements can be brought on this part of the software to make sure that the DAQ can safely  
1101 shutdown at any moment.

1102

#### 1103 **A.6 Software export**

1104 In section A.2 was discussed the fact that the DAQ as written in its last version is not a standalone  
1105 software. It is possible to make it a standalone program that could be adapted to any VME setup  
1106 using V1190A and V1718 modules by creating a GUI for the software or by printing the log mes-  
1107 sages that are normally printed in the webDCS through the log file, directly into the terminal. This  
1108 method was used by the DAQ up to version 3.0 moment where the webDCS was completed. Also, it  
1109 is possible to check branches of DAQ v2.X to have example of communication through a terminal.

1110

1111 DAQ v2.X is nonetheless limited in it's possibilities and requires a lot of offline manual interven-  
1112 tions from the users. Indeed, there is no communication of the software with the detectors' power  
1113 supply system that would allow for a user a predefine a list of voltages to operate the detectors at

| step | actions of webDCS  | status of DAQ  | <code>__runstatuspath</code> |
|------|--|--|------------------------------|
| 1    | launch DAQ<br>ramp voltages<br>ramping over<br>wait for currents stabilization | readout of IniFile<br>configuration of TDCs                                | INIT                         |
| 2    |  | configuration done<br>send DAQ ready<br>wait for START signal              | DAQ_RDY                      |
| 3    | waiting time over<br>send START  |  | START                        |
| 4    | wait for run to end<br>monitor DAQ run status                                  | data taking ongoing<br>check for KILL signal                               | RUNNING                      |
| 5    |  | run over<br>send DAQ_RDY<br>wait for next DCS signal                       | DAQ_RDY                      |
| 6    | ramp voltages<br>ramping over<br>wait for currents stabilization               |  | DAQ_RDY                      |
| 3    | waiting time over<br>send START  |  | START                        |
| 4    | wait for run to end<br>monitor DAQ run status                                  | update IniFile information<br>data taking ongoing<br>check for KILL signal | RUNNING                      |
| 5    |  | run over<br>send DAQ_RDY<br>wait for next DCS signal                       | DAQ_RDY                      |
| 7    | send command STOP  | DAQ shuts down   | STOP                         |

Table A.1: Inter-process communication cycles in between the webDCS and the DAQ through file string signals.

1114 and loop over to take data without any further manual intervention. In v2.X, the data is taken for a  
1115 single detector setting and at the end of each run, the softwares asks the user if he intends on taking  
1116 more runs. If so, the software invites the user to set the operating voltages accordingly to what is  
1117 necessary and to manual update the configuration file in consequence. This working mode can be a  
1118 very first approach before an evolution and has been successfully used by colleagues from different  
1119 collaborations.

1120

1121 For a more robust operation, it is recommended to develop a GUI or a web application to inter-  
1122 face the DAQ. Moreover, to limit the amount of manual interventions, and thus the probability to  
1123 make mistakes, it is also recommended to add an extra feature into the DAQ by installing the HV  
1124 Wrapper library provided by CAEN of which an example of use in a similar DAQ software devel-  
1125 opped by a master student of UGent, and called TinyDAQ, is provided on UGent's github. Then, this  
1126 HV Wrapper will help you communicating with and give instructions to a CAEN HV powered crate  
1127 and can be added into the DAQ at the same level where the communication with the user was made  
1128 in DAQ v2.X. In case you are using another kind of power system for your detectors, it is stringly  
1129 adviced to use HV modules or crates that can be remotely controled via a using C++ libraries.

1130

# B

1131

1132

## Details on the offline analysis package

1133 The data collected in GIF++ thanks to the DAQ described in Appendix A is difficult to interpret by  
1134 a human user that doesn't have a clear idea of the raw data architecture of the ROOT data files. In  
1135 order to render the data human readable, a C++ offline analysis tool was designed to provide users  
1136 with detector by detector histograms that give a clear overview of the parameters monitored during  
1137 the data acquisition [14]. In this appendix, details about this software in the context of GIF++, as of  
1138 how the software was written and how it functions will be given.

### 1139 B.1 GIF++ Offline Analysis file tree

1140 GIF++ Offline Analysis source code is fully available on github at [https://github.com/afagot/GIF\\_OfflineAnalysis](https://github.com/afagot/GIF_OfflineAnalysis). The software requires ROOT as non-optionnal dependency  
1141 as it takes ROOT files in input and write an output ROOT file containing histograms. To compile the  
1142 GIF++ Offline Analysis project is compiled with cmake. To compile, first a build/ directory must  
1143 be created to compile from there:

```
1145 mkdir build
1146 cd build
1147 cmake ..
1148 make
1149 make install
```

1147 To clean the directory and create a new build directory, the bash script cleandir.sh can be used:

```
1148
1149 ./cleandir.sh
```

1150 The source code tree is provided below along with comments to give an overview of the files' con-  
1151 tent. The different objects created for this project (`Infrastructure`, `Trolley`, `RPC`, `Mapping`, `RPCHit`,  
1152 `RPCCluster` and `Inifile`) will be described in details in the following sections.

1153

```

GIF_OfflineAnalysis
├── bin
│   └── offlineanalysis ..... EXECUTABLE
├── build..... CMAKE COMPILATION DIRECTORY
└── ...
    ├── include..... LIST OF C++ HEADER FILES
    │   ├── Cluster.h..... DECLARATION OF OBJECT RPCCLUSTER
    │   ├── Current.h..... DECLARATION OF GETCURRENT ANALYSIS MACRO
    │   ├── GIFTrolley.h..... DECLARATION OF OBJECT TROLLEY
    │   ├── Infrastructure.h..... DECLARATION OF OBJECT INFRASTRUCTURE
    │   ├── IniFile.h..... DECLARATION OF OBJECT INI FILE FORINI PARSER
    │   ├── Mapping.h..... DECLARATION OF OBJECT MAPPING
    │   ├── MsgSvc.h..... DECLARATION OF OFFLINE LOG MESSAGES
    │   ├── OfflineAnalysis.h..... DECLARATION OF DATA ANALYSIS MACRO
    │   ├── RPCTracker.h..... DECLARATION OF OBJECT RPC
    │   ├── RPCHit.h..... DECLARATION OF OBJECT RPCHIT
    │   ├── types.h..... DEFINITION OF USEFUL VARIABLE TYPES
    │   └── utils.h..... DECLARATION OF USEFUL FUNCTIONS
    ├── obj..... BINARY FILES CREATED BY COMPILER
    └── ...
        ├── src..... LIST OF C++ SOURCE FILES
        │   ├── Cluster.cc..... DEFINITION OF OBJECT RPCCLUSTER
        │   ├── Current.cc..... DEFINITION OF GETCURRENT ANALYSIS MACRO
        │   ├── GIFTrolley.cc..... DEFINITION OF OBJECT TROLLEY
        │   ├── Infrastructure.cc..... DEFINITION OF OBJECT INFRASTRUCTURE
        │   ├── IniFile.cc..... DEFINITION OF OBJECT INI FILE FORINI PARSER
        │   ├── main.cc..... MAIN FILE
        │   ├── Mapping.cc..... DEFINITION OF OBJECT MAPPING
        │   ├── MsgSvc.cc..... DECLARATION OF OFFLINE LOG MESSAGES
        │   ├── OfflineAnalysis.cc..... DECLARATION OF DATA ANALYSIS MACRO
        │   ├── RPCTracker.cc..... DECLARATION OF OBJECT RPC
        │   ├── RPCHit.cc..... DECLARATION OF OBJECT RPCHIT
        │   └── utils.cc..... DEFINITION OF USEFUL FUNCTIONS
        ├── cleandir.sh..... BASH SCRIPT TO CLEAN BUILD DIRECTORY
        ├── CMakeLists.txt..... SET OF INSTRUCTIONS FOR CMAKE
        ├── config.h.in..... DEFINITION OF VERSION NUMBER
        └── README.md..... README FILE FOR GITHUB

```

1154

## B.2 Usage of the Offline Analysis

1155

In order to use the Offline Analysis tool, it is necessary to know the Scan number and the HV Step of the run that needs to be analysed. This information needs to be written in the following format:

1157

1158

```
Scan00XXXX_HVY
```

1159

where XXXX is the scan ID and Y is the high voltage step (in case of a high voltage scan, data will be taken for several HV steps). This format corresponds to the base name of data files in the database

1160

1161 of the Gif++ webDCS. Usually, the offline analysis tool is automatically called by the webDCS at  
 1162 the end of data taking or by a user from the webDCS panel if an update of the tool was brought.  
 1163 Nonetheless, an expert can locally launch the analysis for tests on the Gif++ computer, or a user can  
 1164 get the code on its local machine from github and download data from the webDCS for its own anal-  
 1165 ysis. To launch the code, the following command can be used from the `GIF_OfflineAnalysis` folder:

1166  
 1167     `bin/offlineanalysis /path/to/Scan00XXXX_HVY`

1168 where, `/path/to/Scan00XXXX_HVY` refers to the local data files. Then, the offline tool will by itself  
 1169 take care of finding all available ROOT data files present in the folder, as listed below:

- 1170     ● `Scan00XXXX_HVY_DAQ.root` containing the TDC data as described in Appendix ?? (events, hit  
 1171       and timestamp lists), and
- 1172     ● `Scan00XXXX_HVY_CAEN.root` containing the CAEN mainframe data recorded by the monitor-  
 1173       ing tool webDCS during data taking (HVs and currents of every HV channels). This file is  
 1174       created independently of the DAQ.

## 1175     **B.2.1 Output of the offline tool**

### 1176       **B.2.1.1 ROOT file**

1177 The analysis gives in output ROOT datafiles that are saved into the data folder and called using the  
 1178 naming convention `Scan00XXXX_HVY_Offline.root`. Inside those, a list of `TH1` histograms can be  
 1179 found. Its size will vary as a function of the number of detectors in the setup as each set of histograms  
 1180 is produced detector by detector. For each partition of each chamber, can be found:

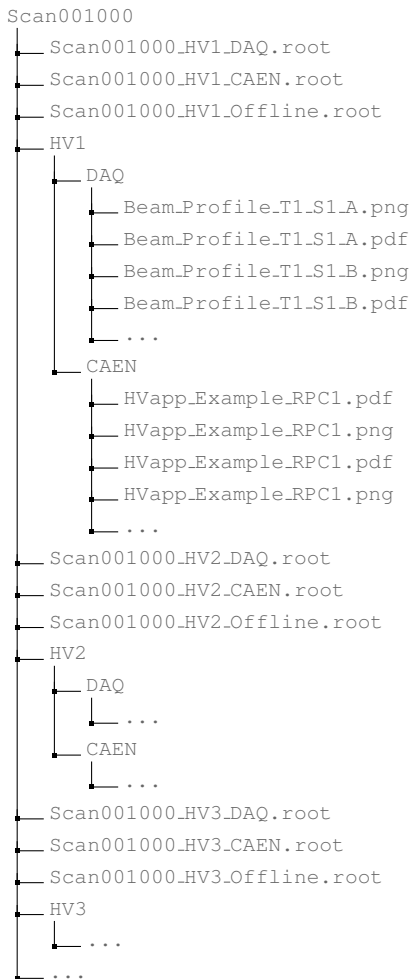
- 1181     ● `Time_Profile_Tt_Sc_p` shows the time profile of all recorded events (number of events per  
 1182       time bin),
- 1183     ● `Hit_Profile_Tt_Sc_p` shows the hit profile of all recorded events (number of events per chan-  
 1184       nel),
- 1185     ● `Hit_Multiplicity_Tt_Sc_p` shows the hit multiplicity (number of hits per event) of all recorded  
 1186       events (number of occurrences per multiplicity bin),
- 1187     ● `Strip_Mean_Noise_Tt_Sc_p` shows noise/gamma rate per unit area for each strip in a se-  
 1188       lected time range. After filters are applied on `Time_Profile_Tt_Sc_p`, the filtered version  
 1189       of `Hit_Profile_Tt_Sc_p` is normalised to the total integrated time and active detection area  
 1190       of a single channel,
- 1191     ● `Strip_Activity_Tt_Sc_p` shows noise/gamma activity for each strip (normalised version of  
 1192       previous histogram - strip activity = strip rate / average partition rate),
- 1193     ● `Strip_Homogeneity_Tt_Sc_p` shows the *homogeneity* of a given partition ( $\text{homogeneity} = \exp(-\text{strip rates standard deviation(strip rates in partition/average partition rate)})$ ),
- 1195     ● `mask_Strip_Mean_Noise_Tt_Sc_p` shows noise/gamma rate per unit area for each masked  
 1196       strip in a selected time range. Offline, the user can control the noise/gamma rate and decide to  
 1197       mask the strips that are judged to be noisy or dead. This is done via the *Masking Tool* provided  
 1198       by the webDCS,

- 1199     ● `mask_Strip_Activity_Tt_Sc_p` shows noise/gamma activity per unit area for each masked  
1200       strip with respect to the average rate of active strips,
- 1201     ● `NoiseCSize_H_Tt_Sc_p` shows noise/gamma cluster size, a cluster being constructed out of  
1202       adjacent strips giving a signal at the *same time* (hits within a time window of 25 ns),
- 1203     ● `NoiseCMult_H_Tt_Sc_p` shows noise/gamma cluster multiplicity (number of reconstructed  
1204       clusters per event),
- 1205     ● `Chip_Mean_Noise_Tt_Sc_p` shows the same information than `Strip_Mean_Noise_Tt_Scp` us-  
1206       ing a different binning (1 chip corresponds to 8 strips),
- 1207     ● `Chip_Activity_Tt_Sc_p` shows the same information than `Strip_Activity_Tt_Scp` using  
1208       chip binning,
- 1209     ● `Chip_Homogeneity_Tt_Sc_p` shows the homogeneity of a given partition using chip binning,
- 1210     ● `Beam_Profile_Tt_Sc_p` shows the estimated beam profile when taking efficiency scan. This  
1211       is obtained by filtering `Time_Profile_Tt_Sc_p` to only consider the muon peak where the  
1212       noise/gamma background has been subtracted. The resulting hit profile corresponds to the  
1213       beam profile on the detector channels,
- 1214     ● `L0_Efficiency_Tt_Sc_p` shows the level 0 efficiency that was estimated **without** muon track-  
1215       ing,
- 1216     ● `MuonCSize_H_Tt_Sc_p` shows the level 0 muon cluster size that was estimated **without** muon  
1217       tracking, and
- 1218     ● `MuonCMult_H_Tt_Sc_p` shows the level 0 muon cluster multiplicity that was estimated **without**  
1219       muon tracking.

1220       In the histogram labels,  $t$  stands for the trolley number (1 or 3),  $c$  for the chamber slot label in  
1221       trolley  $t$  and  $p$  for the partition label (A, B, C or D depending on the chamber layout) as explained  
1222       in Chapter 5.3.

1223       In the context of GIF++, an extra script called by the webDCS is called to extract the histograms  
1224       from the ROOT files. The histograms are then stored in PNG and PDF formats into the correspond-  
1225       ing folder (a single folder per HV step, so per ROOT file). the goal is to then display the histograms  
1226       on the Data Quality Monitoring (DQM) page of the webDCS in order for the users to control the  
1227       quality of the data taking at the end of data taking. An example of histogram organisation is given  
1228       below:

1229



1231     *Here can put some screens from the webDCS to show the DQM and the plots available to users.*  
 1232

1233     **B.2.1.2 CSV files**

1234     Moreover, up to 3 CSV files can be created depending on which ones of the 3 input files were in the  
 1235     data folder:

- 1236       • `Offline-Rate.csv` : contains the summary of the noise/gamma hit and cluster rates for each  
 1237        chamber partitions,
- 1238       • `Offline-Current.csv` : contains the summary of the currents and voltages applied on each  
 1239        RPC HV channel, and
- 1240       • `Offline-L0-EffCl.csv` : contains the summary of the level 0 efficiency and muon cluster  
 1241        information **without** tracking.

1242     Note that these 3 CSV files are created along with their *headers* (`Offline-[...]-Header.csv`  
 1243     containing the names of each data columns) and are automatically merged together when the offline

1244 analysis tool is called from the webDCS, contrary to the case where the tool is runned locally from  
 1245 the terminal as the merging bash script is then not called. Thus, the resulting files, used to make  
 1246 official plots, are:

- 1247     ● Rate.csv ,
- 1248     ● Current.csv ,
- 1249     ● L0-EffCl.csv .

## 1250     B.3 Analysis inputs and information handling

1251 The usage of the Offline Analysis tool as well as its output have been presented in the previous sec-  
 1252 tion. It is now important to dig further and start looking at the source code and the inputs necessary  
 1253 for the tool to work. Indeed, appart from the raw ROOT data files that are analysed, more informa-  
 1254 tion needs to be imported inside of the program to perform the analysis such as the description of  
 1255 the setup inside of GIF++ at the time of data taking (number of trolleys, of RPCs, dimensions of the  
 1256 detectors, etc...) or the mapping that links the TDC channels to the coresponding RPC channels in  
 1257 order to translate the TDC information into human readable data. 2 files are used to transmit all this  
 1258 information:

1259

- 1260     ● Dimensions.ini, that provides the necessary setup and RPC information, and
- 1261     ● ChannelsMapping.csv, that gives the link between the TDC and RPC channels as well as the  
     mask for each channel (masked or not?).

### 1263     B.3.1 Dimensions file and IniFile parser

1264 This input file, present in every data folder, allows the analysis tool to know of the number of ac-  
 1265 tive trolleys, the number of active RPCs in those trolleys, and the details about each RPCs such as  
 1266 the number of RPC gaps, the number of pseudo-rapidity partitions (for CMS-like prototypes), the  
 1267 number of strips per partion or the dimensions. To do so, there are 3 types of groups in the INI file  
 1268 architecture. A first general group, appearing only once at the head of the document, gives informa-  
 1269 tion about the number of active trolleys as well as their IDs, as presented in Source Code B.1. For  
 1270 each active trolley, a group similar to Source Code B.2 can be found containing information about  
 1271 the number of active detectors in the trolley and their IDs. Finally, for each detector stored in slots  
 1272 of an active trolley, there is a group providing information about their names and dimensions, as  
 1273 showed in Source Code B.3.

1274

```
[General]
nTrolleys=2
TrolleysID=13
```

1275     *Source Code B.1: Example of [General] group as might be found in Dimensions.ini. In GIF++, only 2  
     trolleys are available to hold RPCs and place them inside of the bunker for irradiation. The IDs of the trolleys  
     are written in a signle string as "13" and then read character by character by the program.*

```
1277 [T1]
nSlots=4
SlotsID=1234
```

Source Code B.2: Example of trolley group as might be found in `Dimensions.ini`. In this example, the file tells that there are 4 detectors placed in the holding slots of the trolley T1 and that their IDs, written as a single string variable, are 1, 2, 3 and 4.

```
1279 [T1S1]
Name=RE2-2-NPD-BARC-8
Partitions=3
Gaps=3
Gap1=BOT
Gap2=TN
Gap3=TW
AreaGap1=11694.25
AreaGap2=6432
AreaGap3=4582.82
Strips=32
ActiveArea-A=157.8
ActiveArea-B=121.69
ActiveArea-C=93.03
```

Source Code B.3: Example of slot group as might be found in `Dimensions.ini`. In this example, the file provides information about a detector named RE2-2-NPD-BARC-8, having 3 pseudo-rapidity readout partitions. This is a CMS RE2-2 type of detector. This information will then be used for example to compute the rate per unit area calculation.

This information is readout and stored in a C++ object called `IniFile`, that parses the information in the INI input file and stores it into a local buffer for later use. This INI parser is the exact same one that was previously developed for the GIFT++ DAQ and described in Appendix A.5.2.

### 1284 B.3.2 TDC to RPC link file and Mapping

1285 The same way the INI dimension file information is stored using `map`, the channel mapping and mask  
 1286 information is stored and accessed through `map`. First of all, the mapping CSV file is organised into  
 1287 3 columns separated by tabulations (and not by commas, as expected for CSV files as it is easier using  
 1288 streams to read tab or space separated data using C++):

```
1289
1290   RPC_channel      TDC_channel      mask
```

1291 using as formatting for each field:

```
1292
1293   TSCCC      TCCC      M
```

1294 `TSCCC` is a 5-digit integer where `T` is the trolley ID, `s` the slot ID in which the RPC is held insite  
 1295 the trolley `T` and `ccc` is the RPC channel number, or *strip* number, that can take values up to  
 1296 3-digits depending on the detector,

1297 `TCCC` is a 4 digit integer where `T` is the TDC ID, `ccc` is the TDC channel number that can take values  
 1298 in between 0 and 127, and

1299      $M$  is a 1-digit integer indicating if the channel should be considered ( $M = 1$ ) or discarded ( $M = 0$ )  
 1300     during analysis.

1301     This mapping and masking information is readout and stored thanks to the object `Mapping`, pre-  
 1302     sented in Source Code B.4. Similarly to `IniFile` objects, this class has private methods. The first  
 1303     one, `Mapping::CheckIf.NewLine()` is used to find the newline character '`\n`' or return character  
 1304     '`\r`' (depending on which kind of operating system interacted with the file). This is used for the  
 1305     simple reason that the masking information has been introduced only during the year 2017 but the  
 1306     channel mapping files exist since 2015 and the very beginning of data taking at GIF++. This means  
 1307     that in the older files, before the upgrade, the channel mapping file only had 2 columns, the RPC  
 1308     channel and the TDC channel. This method helps controling the character following the readout of  
 1309     the 2 first fields of a line. In case the method finds any end of line character, no mask information is  
 1310     present in the file and the default  $M = 1$  is used. On the contrary, if the next character was a tabulation  
 1311     or a space, the mask information is present.

1312     Once the 3 fields have been readout, the second private method `Mapping::CheckIfTDCCh()` is  
 1313     used to control that the TDC channel is an existing TDC channel. Finally, the information is stored  
 1314     into 3 different maps (`Link`, `ReverseLink` and `Mask`) thanks to the public method `Mapping::Read()`.  
 1315     `Link` allows to get the RPC channel by knowing the TDC channel while `ReverseLink` does the op-  
 1316     posite by returning the TDC channel by knowing the RPC channel. Finally, `Mask` returns the mask  
 1317     associated to a given RPC channel.

```
1318 typedef map<Uint, Uint> MappingData;

class Mapping {
  private:
    bool          CheckIf.NewLine(char next);
    bool          CheckIfTDCCh(Uint channel);
    string        FileName;
    MappingData Link;
    MappingData ReverseLink;
    MappingData Mask;
    int           Error;

  public:
    Mapping();
    Mapping(string baseName);
    ~Mapping();

    void SetFileName(const string filename);
    int Read();
    Uint GetLink(Uint tdcchannel);
    Uint GetReverse(Uint rpcchannel);
    Uint GetMask(Uint rpcchannel);
};
```

1320 *Source Code B.4: Description of C++ object `Mapping` used as a parser for the channel mapping and mask file.*

# C

1321

1322

## Structure of the hybrid simulation software

1323

### C.1 Introduction

1324

insert text here...

